UHASSELT
KNOWLEDGE IN ACTION

Maastricht University

Faculty of Medicine and Life Sciences
School for Life Sciences
Master of Biomedical Sciences

Master's thesis

Schwann cell membrane composition, dynamics and interactions with their micro-environment in Charcot-Marie-Tooth disease type 1A: a patient-in-a-dish model approach

Koen Kuipers

Thesis presented in fulfillment of the requirements for the degree of Master of Biomedical Sciences, specialization Molecular Mechanisms in Health and Disease

SUPERVISOR :

Prof. dr. Ivo LAMBRICHTS

MENTOR :

dr. Tim VANGANSEWINKEL

2021
2022

Transnational University Limburg is a unique collaboration of two universities in two countries: the University of Hasselt and Maastricht University.

UHASSELT
KNOWLEDGE IN ACTION

www.uhasselt.be
Universiteit Hasselt
Campus Hasselt:
Martelarenlaan 42 | 3500 Hasselt
Campus Diepenbeek:
Agoralaan Gebouw D | 3590 Diepenbeek

UHASSELT
KNOWLEDGE IN ACTION

Maastricht University

Faculty of Medicine and Life Sciences
School for Life Sciences
Master of Biomedical Sciences

Master's thesis

Schwann cell membrane composition, dynamics and interactions with their micro-environment in Charcot-Marie-Tooth disease type 1A: a patient-in-a-dish model approach

Koen Kuipers

Thesis presented in fulfillment of the requirements for the degree of Master of Biomedical Sciences, specialization Molecular Mechanisms in Health and Disease

SUPERVISOR :

Prof. dr. Ivo LAMBRICHTS

MENTOR :

dr. Tim VANGANSEWINKEL

Schwann cell membrane composition, dynamics and interactions with their micro-environment in Charcot-Marie-Tooth disease type 1A: a patient-in-a-dish model approach*

Kuipers K.[1], Vangansewinkel T.[1,2], Jeurissen H. [1], Libberecht K.[1,2] ,Hasevoets S. [1], Vanherle S. [3], Loix M.[3], Bogie J. [3], Wolfs E. [1] and Lambrichts I.[1]

[1] Department of Cardio and Organ Systems, Biomedical Research Institute, Hasselt University, Diepenbeek, Belgium.
[2] VIB, Center for Brain & Disease Research, Laboratory of Neurobiology, Leuven, Belgium.
[3] Department of Immunology, Biomedical Research Institute, Hasselt University, Diepenbeek, Belgium.

*Running title: *Cell membrane changes in CMT1A Schwann cell models*

To whom correspondence should be addressed: Prof. dr. Ivo Lambrichts, Tel: +32 (11) 26 92 45; Email: ivo.lambrichts@uhasselt.be

Keywords: Charcot-Marie-Tooth disease type 1A; peripheral nervous system; Schwann cell; integrins; lipid metabolism; lipid raft; extracellular matrix

ABSTRACT

Charcot-Marie-Tooth disease type 1A (CMT1A) is the most common inherited peripheral neuropathy, affecting motor and sensory function in patients. CMT1A is triggered by a *PMP22*-gene duplication resulting in dysmyelination in Schwann cells. Schwann cell myelination depends on interactions with the endoneurium, effectuated mainly via integrin receptors on the abaxonal membrane. Therefore, our aim was to determine integrin expression profiles and lipid characteristics in CMT1A Schwann cells. CMT1A patient induced pluripotent stem cell derived Schwann cell precursors (iPSC-SCPs) and PMP22-transduced human dental pulp stem cells (DPSCs) were used to model CMT1A *in vitro*. The following analysis were performed: immunocytochemistry and qPCR to measure and correlate integrin and PMP22 levels, spectral imaging with environmental sensitive dyes on giant plasma membrane vesicles (GPMV) to study membrane polarity, ganglioside GM1 labelling to explore lipid raft properties, BODIPY-lipid droplet labelling, and cell migration and hydrogel contraction assays to study cell-ECM interactions. We found that the integrin α6, β1 expression levels are significantly decreased in CMT1A iPSC-SCPs compared to isogenic controls, but significantly increased in PMP22-overexpressing DPSCs. Additionally, integrin receptor mRNA levels were altered in iPSC-SCPs. Spectral imaging with Di-4-ANEPPDHQ and Laurdan showed significantly decreased membrane polarity in CMT1A GPMVs. Live cell-imaging of lipid rafts revealed lower raft mobility in CMT1A. BODIPY labelling highlighted a decreased lipid droplet presence. Finally, migration of CMT1A iPSC-SCPs in 2D was significantly reduced. Conclusively, we found altered integrin expression and (membrane) lipid properties in our CMT1A models, highlighting a disturbed cell-ECM axis and a pivotal contribution towards CMT1A dysmyelination.

INTRODUCTION

In the first half of 1886, multiple cases of progressive peroneal muscular atrophy were described by the French neurologist Jean-Martin Charcot and his student Pierre Marie, and Henry Tooth independently. Later, this disease was named Charcot-Marie-Tooth disease (CMT), based on a consensus reached by other researchers in the field of neurology (1). CMT, also known as hereditary motor and sensory neuropathy (HMSN), is a group of inherited peripheral nervous system (PNS) diseases affecting approximately 1 in 2500 people (2). CMT can be divided into demyelinating (CMT1), axonal (CMT2) or intermediate types; Additional subtypes of CMT are named with a letter, representing a specific gene that underlies the CMT phenotype (such as CMT1A (*PMP22* duplication, see below), CMT1B (*MPZ* mutations),

and CMT2B (*RAB7A* gene alterations) for example) (3). Currently, the golden standard for CMT diagnosis is the combination of nerve-conduction studies, clinical examination and genetic testing (4). The most prevalent form of CMT is CMT1A, representing 60% to 70% of all CMT patients, and is therefore studied most in the context of CMT to ultimately identify treatment targets (2, 5). CMT1A is caused by a 1.5-megabase (Mb) duplication on chromosome 17p11.2. This duplication contains the *Peripheral myelin protein 22* (*PMP22*)-gene, which is considered to be the cause of the disease by means of an increased gene dosage (5, 6). The PMP22-duplication in CMT1A patients leads to a general hypomyelination of peripheral nerves, shorter internodes, some de- and hypermyelinated nerves, myelin sheath defects, axonal loss and decreased intraepidermal small fiber density (7, 8). CMT1A patients typically suffer from a distally progressing muscle weakness and atrophy, and sensory loss in the limbs. These symptoms usually manifest first in the lower legs, and later also affect the arms (2). Cardinal signs seen in most CMT1A patients are pes cavus — arching of the foot — and hammertoes (2, 9). Additionally, in the vast majority of CMT1A patients, pain is also a life hindering symptom (10). Convergently, these physical symptoms are a major contributor to the decreased quality of life seen in CMT patients (11-13). Despite being known for more than 130 years, thus far, the underlying pathobiology of CMT1A remains largely unknown. Currently, a few clinical trials are attempting to treat CMT1A with some positive results. However, no effective CMT1A treatments have been approved yet, and patients typically rely on symptomatic and supportive care by means of surgical corrections and physical therapy (2, 5).

Upon investigation of the peripheral nerves in CMT1A patients, histological onion-bulb structures can be observed. These structures contain a central hypomyelinated nerve with encircling supernumerary Schwann cells (14, 15). Myelin is a multilamellar structure formed by spiral wrapping of the Schwann cell plasma membrane around axons. Under physiological circumstances, Schwann cells have the propensity to myelinate PNS neurons with an axonal diameter larger than ~1 µm to ultimately increase action potential propagation efficiency via saltatory conduction (16, 17). Schwann cells are the main cell type that express PMP22, a tetraspan membrane protein, and integrate PMP22 into their myelin sheath; PMP22 comprises around 2-5% of all myelin proteins (18). Folding and trafficking of PMP22 occurs inefficiently in healthy conditions, leading to only 20% of newly expressed protein being trafficked to the cell surface (19). Despite being characterized as a myelin transmembrane protein, the exact functions of PMP22 have yet to be defined. Nevertheless, PMP22 has been proven to contribute to Schwann cell growth and differentiation, myelin stabilization, establishment of lipid rafts, cholesterol trafficking and has recently been detected in close proximity of Lamin-B1 in peripheral nuclear regions (2, 20-22). In two commonly used CMT1A mouse models, Trembler-J (TrJ) and C22 mice, a decrease in PMP22 turnover rate is observed (14, 23, 24). Additionally, upon induction of an increased expression of PMP22, the amount of intracellular PMP22 increases more than the amount of surface-trafficked protein does (19). Consequently, an increase in perinuclear protein aggregates is also observed in CMT1A Schwann cells, containing PMP22 that is misfolded due to its overexpression (23-25).

Schwann cells are very heavily dependent on their interactions with extracellular matrix (ECM) molecules. These ECM components — including collagen (I, IV), fibronectin, laminin heterotrimers, and proteoglycans— are required for proper development, ensheathment and myelination of PNS axons (26, 27). Initially, neural crest cells (NCC) delaminate from the neural epithelium of the neural tube during neurulation. Disorders arising by means of disturbances in the differentiation and migration, as well as abnormal expression and NCC death are classified as neurocristopathies, classically including the CMT variants (28). A major subpopulation of NCCs eventually migrate along PNS axons as Schwann cell precursor (SCP) cells, whereas other NCCs form a group of boundary cap cells, located on the central nervous system (CNS)-PNS transition (29). Next, SCPs differentiate towards an immature Schwann cell (iSC) state, leading to cessation of cell migration. These iSCs start the formation of an extensive basal lamina and start sampling surrounding axons in the process of radial sorting. During radial sorting, an iSC establishes a 1:1 relationship with a single larger diameter axon and becomes a pro-myelinating Schwann cell (pro-SC). Smaller axons

do not take part in radial sorting and they slowly associate with iSCs by forming remak bundles that nest themselves in membrane cavities of Remak Schwann cells. pro-SCs subsequently differentiate gradually towards myelinating Schwann cells, availing themselves of signals from its ECM micro-environment and the encompassed axon/neuron (27, 30). Within this differentiation process, and Schwann cell phenotype preservation, the basal lamina plays a crucial role via receptor communication on the abaxonal Schwann cell membrane. A pivotal receptor family in this process, is the integrin receptor family. Integrins are a family of surface transmembrane receptors that mediate cell-cell or cell-ECM adhesion. Generally, integrins form heterodimeric receptor complexes composed of an alpha and beta subunit, non-covalently associated and are membrane spanning (31). Upon cell or ECM interaction, integrins can mediate mechanical positioning of the cell, as well as transmit intracellular signals; Pathways involved in integrin signaling result in cytoskeletal organization, protein phosphorylation, calcium oscillations or gene expression (31, 32). In Schwann cells, integrin α6β1 and α6β4 heterodimeric receptors are both important in Schwann cell development and myelination (32). Integrin α6β1 interacts with laminin 211 and 411, mediating radial sorting signaling in mouse dorsal root ganglion (DRG) Schwann cells. In the absence of integrin α6β1, integrin α7β1 can compensate for its loss. However, absence of either complexes leads to impairment of Schwann cell cytoplasmic extension and binding to laminin 211 and 411 (33). Additionally, integrin α5β1 interacts with fibronectin, and is expressed most during Schwann cell development and peripheral nerve regeneration (34). Interestingly, integrin β1 receptors that do not actively interact with laminin are proposed to also contribute to radial sorting through pathways that have yet to be further specified (33). However, integrin β1 on its own does mediate Schwann cell process extension and radial lamellae formation in radial sorting through Rac1 (35). In aged mice, integrin α6β4 deficiency leads to abnormal myelin sheath folding (36). Integrin α6β4 is found in complex with PMP22, potentially contributing to the CMT1A pathophysiology (35). In PMP22$^{-/-}$ mouse DRG, Schwann cell integrin β4 protein levels are strongly reduced. However, contrary to this finding, in PMP22 mutant mice, integrin β4 levels remain unchanged, implying that there is a correlation between *PMP22* gene dosage and integrin β4 expression (14). The function of integrin α6 in Schwann cells, despite being part of the integrin α6β1 and α6β4 complexes, has thus far not been determined (35). Additionally, the exact contribution of integrin α6β1 and α6β4, as well as their interaction with PMP22, in CMT1A has heretofore not been described. Nevertheless, transcriptomic pathway analyses on Schwann cells with either overexpression or knockout of *PMP22* do show major alterations in ECM interaction and degradation pathways (37).

Aside from membrane protein interactions, there are other important (direct and indirect) factors in the Schwann cell communication with its micro-environment, such as cellular lipid metabolism, cell membrane lipid composition and lipid raft dynamics. Schwann cells are heavily dependent on their lipid production to form and maintain their myelin sheath. Myelin generally consists of a high proportion of lipids (70-85%); The most abundant lipids in the PNS myelin are cholesterol (41%), phospholipids (29%) and sphingomyelin (13%) (38). Alterations in these lipids are evident in DRG from CMT rats, where drastic changes in phospholipid, sphingolipid and cholesterol metabolism are seen that can mostly be reversed by a lipid-enriched diet or supplementation of substrates for these specific metabolic pathways (39, 40). A lipid raft is a canonical term that is used to describe a combination of cholesterol, glycosphingolipids, and various proteins organized in a detergent-insoluble membrane lipid microdomain (20). Despite its essential contribution in the cell-ECM interaction axis, the exact function of a lipid raft in biology still remains a mystery to this day (41). In Schwann cells, PMP22 has been localized to these cholesterol-enriched lipid rafts (20). PMP22$^{-/-}$ mice do not properly develop their F-actin-enriched Schmidt-Lanterman incisures, and expression and localization of lipid raft associated molecules like flotillin-1, cholesterol, and GM1 ganglioside are altered (20). Within lipid rafts, PMP22 interacts with ATP-binding cassette transporter A1 (ABCA1), a cholesterol and phospholipid efflux transporter. PMP22-deficient Schwann cells have both an increase in mRNA and protein levels of

ABCA1 and apolipoprotein E (apoE). However, despite their upregulation in expression, the localization of ABCA1 towards the cell membrane and apoE secretion is reduced (21). Additionally, in CMT1A fibroblasts, increased cholesterol and PMP22 quantities are found in lysosomes, and triglyceride and cholesterol synthesis-associated genes are upregulated (42). Other *PMP22* mutations, found in TrJ mice and mice with mutations in the *PMP22* cholesterol-binding CRAC-motif, show a different PMP22 and cholesterol distribution. In both these models, PMP22 is retained in the endoplasmic reticulum and Golgi apparatus. Moreover, *PMP22* CRAC-motif mutations lead to cholesterol displacement into the Golgi apparatus as well (42). In sural nerve biopsies of CMT1A patients, a change in sphingolipid and glycerophospholipid metabolism has also been observed, contributing to myelin deficiencies (39, 40). Furthermore, pathway analysis on primary Schwann cells with a lentiviral-induced PMP22 overexpression reveals major alterations in fatty acid metabolism and fatty acid chain elongation pathways (37). Altogether, these studies indicate that changes in PMP22 lead to an altered cellular lipid metabolism, cell membrane lipid composition, and lipid raft formation and dynamics through a multitude of pathways.

Frequently used *in vitro* models to study CMT1A have thus far mostly been primary Schwann cells derived from the C22 or C3-PMP22 mouse model or the CMT rat model (43, 44). Due to ethical and practical limitations, human Schwann cell *in vitro* models have not been used in CMT1A research. To overcome these barriers, a few recent studies have proposed induced pluripotent stem cell iPSC differentiation protocols that result in Schwann cell-like cells (45). Furthermore, we have been able to differentiate human dental pulp stem cells (DPSCs) into myelinating Schwann cells in our lab (DPSC-SCs) (46). However, to our knowledge, no previous studies have used any of these human *in vitro* models to study the CMT1A pathobiology. Therefore, iPSC-Schwann cell precursor-like (iPSC-SCP, henceforth also referred to as SCPs) cells, as well as PMP22-overexpressing DPSCs (DPSC-PMP22), were used in this study to enhance our understanding of the CMT1A pathobiology in this study. To further minimize the limitations of 2D cell culture experiments, we have previously developed both a free-floating and aligned cell-embedded collagen 1 hydrogel model that mimics the 3D cellular environment (47). By placing cells in a 3D endoneurium-like environment, Their behavior resembles their *in vivo* behavior more closely and more accurate analyses on ECM-receptor interactions with their ECM microenvironment can be done (48, 49). The relevance of the abovementioned 3D model is foregrounded through the fact that the PNS is constantly under daily biomechanical stress without degenerating the peripheral nerves, facilitated partly through mechanical support of the ECM. PMP22 deficiencies not only lead to CMT1A, but also hereditary neuropathy with liability to pressure palsies (HNPP), a disease characterized by increased PNS sensitivity to mechanical forces (16). Therefore, we have used both 2D and 3D cell cultures in the present study to obtain more detailed insights in cell-ECM biomechanical communication.

The **aim of this study** is to further specify the changes in CMT1A Schwann cell membranes, more specifically its biomechanical interactions with the ECM through integrin receptors, membrane lipid properties, lipid raft dynamics, phospholipid and cholesterol metabolism alterations, cellular lipid retention in lipid droplets and Schwann cell precursor dynamics in an endoneurium-like environment. I **hypothesize** that the overexpression of PMP22 interferes with integrins, membrane lipid composition and dynamics, phospholipid and cholesterol metabolism, and general cell-ECM interaction in multiple *in vitro* Schwann cell models for CMT1A. A summary of the hypothesis is given in Fig. 1. To test our hypothesis, we first performed immunocytochemistry staining experiments and qPCR on iPSC-SCP and DPSC-PMP22 cells to determine integrin and PMP22 expression levels and their colocalization in CMT1A cellular models. Next, we used giant plasma membrane vesicles (GPMV) as a plasma membrane-proxy to determine the cell membrane polarity in CMT1A iPSC-SCPs using Laurdan and Di-4-ANEPPDHQ labelling techniques. Subsequently, we examined PMP22-lipid raft expression and colocalization, as well as lipid raft dynamics in iPSC-SCPs using temporospatial live cell imaging. To increase our understanding of the changes in phospholipid and cholesterol metabolism in CMT1A, we next performed RNA sequencing and mass spectrometry

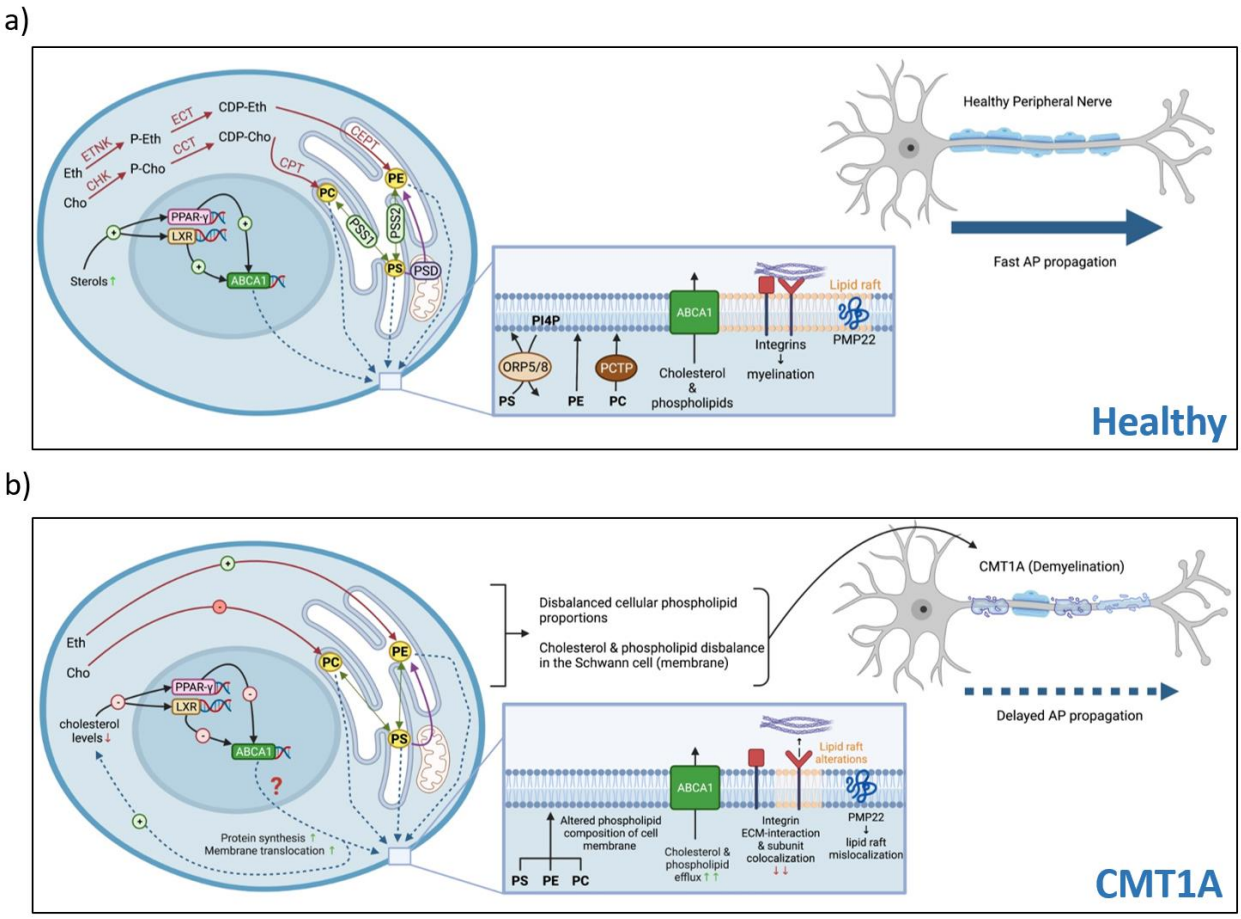

Figure 1 – **Graphic hypothesis overview|** a) Phospholipid biosynthesis, membrane lipid incorporation, efflux of phospholipids and cholesterol, membrane lipid raft domains and integrin-ECM signalling in healthy Schwann cells. Phosphatidylcholine (PC) and phosphatidylethanolamine (PE), the dominant cellular phospholipid species, are synthesized via the Kennedy pathway (**red**). Phosphatidylserine (PS) is synthesized from PC and PE in the endoplasmic reticulum (**green**). PS can also be converted to PE through PSD in mitochondria (**purple**). Normally, reduced phospholipid and cholesterol levels reduce ABCA1 expression through PPARγ and LXR. PCTP, ORP5 and ORP8 incorporate PS and PC into the cell membrane, while PE is not incorporated via transfer proteins. PMP22 and most integrins are generally contained in lipid rafts, where colocalization between integrin subunits can occur. Integrins are essential abaxonal ECM-receptors. b) Our hypothesis is that in CMT1A, phospholipid synthesis is dysregulated, leading to altered membrane lipid composition. CMT1A Schwann cells have an increased cholesterol efflux rate; Despite close regulation of ABCA1 through PPARγ and LXR, the increase in cholesterol efflux (primarily via ABCA1) persists through an unknown mechanism. Additionally, CMT1A Schwann cells have dysregulated lipid raft dynamics, integrin subunit colocalization and ECM-interactions, all leading to the altered Schwann cell phenotype seen in CMT1A. Eth = ethanolamine; Cho = choline; ETNK = ethanolamine kinase; CHK = choline kinase; P-Eth = phosphoethanolamine; P-Cho = phosphocholine; ECT = CTP:phosphoethanolamine cytidylyltransferase; CCT = CTP:phosphocholine cytidylyltransferase; CDP-Eth = CDP-ethanolamine; CDP-Cho = CDP-choline; CEPT = choline/ethanolaminephosphotransferase; CPT = choline phosphotransferase; PSS1 = phosphatidylserine synthase 1; PSS2 = phosphatidylserine synthase 2; PPARγ = peroxisome proliferator-activated receptor; LXR = liver X receptor; ABCA1 = ATP-binding cassette transporter 1; ORP5 = oxysterol-binding protein-related protein 5; ORP8 = oxysterol-binding protein-related protein 8; PCTP = phosphatidylcholine transfer protein; AP = action potential.

on iPSC-SCPs, as well as cholesterol flux experiments and a GPMV experiment using multiple lipid metabolism altering compounds. Additionally, we analyzed iPSC-SCP lipid storage by means of neutral lipid BODIPY-labelling. Finally, we used free-floating collagen I hydrogel experiments, observing both macroscopic and

microscopic alterations, as well as membrane protein characteristics.

EXPERIMENTAL PROCEDURES

iPSC-SCP cell culture – A human CMT1A patient-derived iPSC lines (67i) and the TALEN corrected isogenic (ISO) control of this line were used (kindly provided by Dr. Robert H. Baloh, Center for Neural Science and Medicine, Los Angeles, USA). Differentiation of iPSCs towards Schwann cell precursor-like cells (iPSC-SCP) was done in the lab of prof. dr. Ludo Van Den Bosch (VIB/KULeuven). iPSC-SCPs were kept in Corning® Matrigel®-coated T75 culture flasks using a custom iPSC-SCP medium, consisting of a 1:1 mix of DMEM-F12 medium (10565018, ThermoFisher) and Neurobasal medium (21103049, ThermoFisher), supplemented with 0.005% BSA-solution (11930, Enzo Life Sciences BVBA), 2mM GlutaMAX™ (35050061, ThermoFisher), 100 U/ml Penicillin & streptomycin (15140122, ThermoFisher), 1x N2 supplement (15140122, ThermoFisher), 1x B27 supplement without vitamin A (12587010, ThermoFisher), 20 µM SB431542 (1614, Tocris), 3mM Chir 99021 (4423, Tocris), 0.11 mM β-mercapto-ethanol (Thermo Fisher Scientific) and 25 ng/ml Neuregulin (100-03, Peprotech), and were kept in a humidified incubator at 37°C and 5% CO_2. Medium was changed 3x per week. At ±80-90% cell confluency, cells were retrieved using accutase® and harvested for further use. A total of 5000 cells (cholera toxin B Alexa Fluor 488 live cell imaging; µ-slide 8-well plate [Ibidi]) 10 000 cells (ICC, 24 well-plate), 30 000 cells (qPCR, 24 well-plate; Amplex/Efflux/FACS, 96 well-plate) were seeded on Corning® Matrigel® for subsequent experiments. In our lipid metabolism altering conditions GPMV experiment, either H_2O (control), 1 µM Choline chloride, 1µM Methyl-ß-cyclodextrin, 10 µg/ml Soybean or 100 µg/ml human central nervous system (CNS) myelin (kindly provided by Prof. Bogie, UHasselt) was administered to the cell cultures 24 hours before GPMV induction. Final working solutions were administered 1/100 (prepared in H_2O) to the culturing medium to reach the above concentrations.

Immunocytochemical staining – Cells were fixed with 4% paraformaldehyde (PFA) in PBS for 20 min and subsequently permeabilized with 0.05% Tween 20. Next, cells were washed in PBS and blocked with 10% blocking solution (Agilent Dako). Primary antibodies were added in the concentration mentioned in table 1 and left to incubate overnight at 4°C. Afterwards, secondary antibodies (Supplementary Table 1) were added (1/300 dilution in PBS) and incubated for 2 hours at room temperature (RT). Nuclei were counterstained with DAPI (1/10000, Thermo Fisher Scientific) for 10 min at RT. Cells were mounted using Thermo Scientific Shandon Immunomount™. Images were taken with a Leica fluorescence microscope (DM 4000 B LED) with the Leica Application Suite X software and analyzed using the Fiji software version 2.1.0/1.53p (Rasband, W.S., ImageJ, U.S. National Institutes of Health, Bethesda, Maryland, USA). Quantitative analysis was performed on the original raw image files. Mander's coefficient was determined using the Coloc2 plugin (PSF = 3; 10 Costes' randomisations). To enhance readability, both contrast and brightness of images were adjusted to an equal degree in the representative images of both CMT1A and control cell groups.

Cholera toxin B AF488 staining – Lipid rafts in cells were stained using the Vybrant® Alexa Fluor® 488 Lipid Raft Labelling Kit (Thermofisher Scientific), according to the manufacturer's protocol. Temporospatial recordings of lipid rafts were visualized and made using live cell TIRF imaging on an in-house Zeiss Elyra PS.1 widefield fluorescence microscope (Alpha Plan-Apochromat 100x/1.46 oil DIC M27). 1000 images (Resolution 512x512) were taken with intervals of 34 milliseconds.

Giant Plasma Membrane Vesicles (GPMVs) – As a model of the cell membrane lipid structure, GPMVs were generated from iPSC-SCP cultures (ISO/CMT1A) according to the protocol described by Sezgin et al (50, 51). In brief, cells are grown in culture flasks (>90%) until confluence and washed with PBS and GPMV buffer (150 mM Sodium Chloride, 10 mM N-(2-Hydroxyethyl)piperazine-N'-(2-ethanesulfonic acid) (HEPES, Sigma-Aldrich), 2mM Calcium Chloride (Sigma-Aldrich) in MilliQ; pH=7.4). Next, GPMV buffer supplemented with 25mM PFA and 10 mM Dithiothreitol (DTT) (i.e. vesiculation forming agents) was administered on top of cells for 2h in a humidified incubator at 37°C and 5% CO_2. In this

time frame, GPMVs are formed and released in the buffer/supernatant.

GPMVs were labeled with either Laurdan or Di-4-ANEPPDHQ through supplementation (0.4 µM in PBS at room temperature). Spectral imaging was done using a Zeiss LSM880 microscope with a 32-channel gallium arsenide phosphide (GaAsP) detector array. Resolution of the images were set at 512x512 pixels (Pixel dwell time: 0.85µs; Scan time: 521.01 ms). Excitation of Laurdan and Di-4-ANEPPDHQ was done at 405 nm (MaiTai laser, Two-photon excitation) and 488 nm, respectively. Generalized polarization (GP) values [-1,+1] for Laurdan and Di-4-ANEPPDHQ were calculated based on the obtained emission wavelengths (Laurdan: GP = (I440 – I490)/(I440 + I490); Di-4-ANEPPDHQ: GP = (I560-I650)/(I560+I650)). The custom-written Matlab protocol for GPMV data analysis (average GP value and phasor plots) was performed in cooperation with prof. dr. Martin vandeVen (research group NEURO, Biomedical Research Institute).

Collagen I hydrogel matrix – Hydrogels are prepared by mixing 10x MEM (Sigma-Aldrich) and type I rat tail collagen (First Link UK; 2 mg/ml in 0.6% acetic acid) in a 1:8 ratio. pH of the hydrogel was adjusted using 1M NaOH (pH≈7.4) and cells were seeded in the gel (density: 10^6 cells/ml). Free-floating hydrogels were casted in a 96 well plate and left in a humidified incubator for 1 hour to let the collagen I polymerize. Cells were imaged at regular time points (0, 3, 24, 48h) both macro- and microscopically. Macroscopic images were made using a Sony Handycam (HDR-XR350). Microscopic images were made using an inverted phase-contrast microscope (Nikon, Eclipse TS100, Nikon, Japan). At the endpoint, two-photon excitation (TPE) microscopy in the form of Second Harmonic Generation (SHG) and cellular autofluorescence was performed (pixel dwell time: 1.02 µs; Scan time: 10.07s) to visualize the cells and collagen I fibrils. Collagen I alignment was quantified using a custom Matlab script in cooperation with prof. dr. Martin vandeVen (research group NEURO, Biomedical Research Institute), based on the method describe by Sanen et al (47).

BODIPY-labelling of neutral lipids – For FACS: medium was removed from cells, rinsed once with PBS and labelled with 2 µM 4,4-Difluoro-1,3,5,7,8-Pentamethyl-4-Bora-3a,4a-Diaza-s-Indacene (BODIPY; Thermofisher Scientific) for 15 min at 37 °C in the dark. An unstained control was included. BODIPY-solution was then removed, and cells were kept in PBS until Flow cytometry was performed for BODIPY labelling analysis. For ICC: After cell fixation and permeabilization, 20 µM BODIPY was administered for 1 hour. Standard ICC protocol was subsequently followed.

Quantitative PCR – RNA isolation was done according to the detailed protocol described in the Supplementary Materials. A qPCR mastermix was prepared using SYBR green (Applied Biosystems) and targeted primers (Supplementary Table 2). 7,5 µl of qPCR mastermix was added to 2,5 µl of the cDNA samples onto the PCR-plate, with milliQ blancs as negative control. After short plate centrifugation at 1200 rpm, the qPCR reaction was started using the Quantstudio 3 RT-PCR system (Thermo Fisher) with a holding stage at 95°C for 20 seconds, a cycling stage at 95°C for 3 seconds and 60°C for 30 seconds, repeated 40 times, and a melt curve stage at 95°C for 15 seconds, 60°C for 1 min and 95°C for 15 seconds again. The samples were analyzed using the Quantstudio software (Thermo Fisher). GAPDH and RPL13A [1], and YWHAZ and CYCA [2] were used as internal controls in the analysis of iPSC-SCPs [1] and DPSCs [2].

Statistical analysis – Prior to the analysis, data were checked for normality using the Shapiro-Wilk test. Data following a normal distribution were analyzed using a Student's *t* test (2 groups) or ANOVA with post-hoc Tukey's multiple comparison test. Not-normally distributed data were analyzed using a Mann-Whitney U test. MANOVA analysis with post hoc Eta Squared test was done using Rstudio Desktop 2022.02.2+485. All other statistical analyses were performed using Graphpad (Prism) version 9.3.1 (471). All graphs were made with the software used in their statistical analysis (Graphpad/Rstudio).

RESULTS

CMT1A iPSC-SCPs and DPSC-PMP22s display distinct expression and colocalization patterns of integrin receptors – As a first step, we checked whether PMP22 overexpression affects ECM receptors in iPSC-SCPs and DPSCs, two Schwann cell *in vitro* models. Supplementary Figure 1 provides a brief summary of the morphology and several Schwann cell lineage

markers describing the iPSC-SCP model used in this study. Integrin α6 and β1 integrated density levels in immunocytochemistry images reveal that SCPs have significantly lower expression levels of both integrin receptors (Fig. 2a,c,d). However, integrin β4 expression remains indifferent between isogenic and CMT1A groups (Fig. 2b,e). Additionally, iPSC-SCPs have a significantly increased PMP22 expression (~1.3x increase). Despite a similar decrease in integrin α6 and β1 expression levels, colocalization of integrin α6 with β1 is strongly decreased in CMT1A cells (Fig. 2g). However, no difference is seen in integrin β1 colocalization with integrin α6 (Fig. 2g). qPCR analysis on 2D-cultured SCPs further confirms the decrease in integrin α6 and β1 expression at the transcriptomic level, as well as in the expression of integrin α5 and α7 (Fig. 2h). Contrary to the ICC results, PMP22 mRNA levels were significantly decreased in CMT1A SCPs (Fig. 2h) despite having an extra duplication of the *PMP22* gene (data not shown, unpublished ddPCR data of the research group of prof. dr. Ludo van den Bosch [VIB/KULeuven]). Levels of Hippo-pathway transcripts (YAP-1, TAZ), focal adhesion transcripts (FAK, PXN), choline transporter CTL1 and cell adhesion molecule CADM4 remained unaltered (Fig. 2h). 3D-cultured SCPs in a free-floating collagen I hydrogel (2mg/ml) — further described in the methods section — only revealed a significant decrease in integrin α6 mRNA levels in CMT1A versus isogenic cells (Fig. 2i). Analysis of the relative expression differences of the transcripts in 2D and 3D-cultured SCPs (Fig 2h,i) in the CMT1A group reveals that integrin α5 is strongly increased and that integrin α6 is significantly decreased in 3D-cultured cells compared to 2D, indicating that characteristics of the cellular micro-environment influences SCP integrin mRNA expression. Furthermore, YAP-1 mRNA levels shows a trend towards relatively higher expression levels in 3D cultured CMT1A SCPs while TAZ (another Hippo pathway regulator) is significantly increased when cells are cultured in 3D. Additionally, mRNA levels of FAK and CADM4 are also significantly higher in CMT1A cells cultured in 3D.

In the DPSC-PMP22 *in vitro* model, similar experiments were performed. Notably, integrin α6, β1 and β4 integrated density levels were significantly increased in DPSC-PMP22s (Fig. 3a-e), however PMP22 expression levels remain unaltered between the DPSC and DPSC-PMP22 groups on the protein level (Fig. 3f). Manders' colocalization analysis reveals an increased colocalization between integrin β1 with α6. PMP22 is also found significantly more in colocalization with integrin β4, however, integrin β4 is strongly reduced in its colocalization with PMP22 (Fig. 3g). Finally, qPCR analysis on 2D-cultured DPSC, with or without PMP22 overexpression, does not reveal any significant changes in target gene expression levels (Fig. 3h). Nevertheless, a trend towards an increased expression of PMP22 and integrin α7 and a decrease in integrin α6, YAP-1, TAZ, FAK and PXN was observed on the mRNA levels in DPSC-PMP22s.

Spectral analysis on Laurdan- and Di-4-ANEPPDHQ labeled GPMVs indicate reduced membrane polarity in CMT1A Schwann cells. - GPMVs are cell membrane-derived vesicles, representing the host cell membrane lipid and protein profile. Laurdan and Di-4-ANEPPDHQ are both membrane-embedded fluorescent molecules that can give an indication of the relative levels of membrane lipid packing and membrane ordering (51). By retrieving GPMVs from iPSC-SCPs and subsequent Laurdan- and Di-4-ANEPPDHQ staining, a generalized polarization (GP) value can be obtained from the emission spectra of these probes (Fig. 4a). Di-4-ANEPPDHQ labelling of SCP GPMVs reveals a decrease in the CMT1A GP value (Fig. 4b-d). Examination of the GP area graphs reveals a singular peak distribution in the CMT1A group. A similar peak is also seen in the isogenic GPMVs, however, this is accompanied by a second peak at higher GP-values (~0.2) (Fig. 4e). Furthermore, multivariate ANOVA (MANOVA) analysis indicates that there is a large effect of ISO-CMT1A grouping on the population differences observed in the phasor plot (Fig. 4f). However, to what degree this can be translated biologically, is on its own difficult to address. Laurdan labelling of SCP GPMVs also reveals a strong decrease in CMT1A GP value, correlating with a higher level of disordering in the cell membrane of CMT1A Schwann cells (Supplementary Fig. 2a-c). The area graph represents a more widespread distribution in GP values compared to the CMT1A area peak, shifting towards more positive

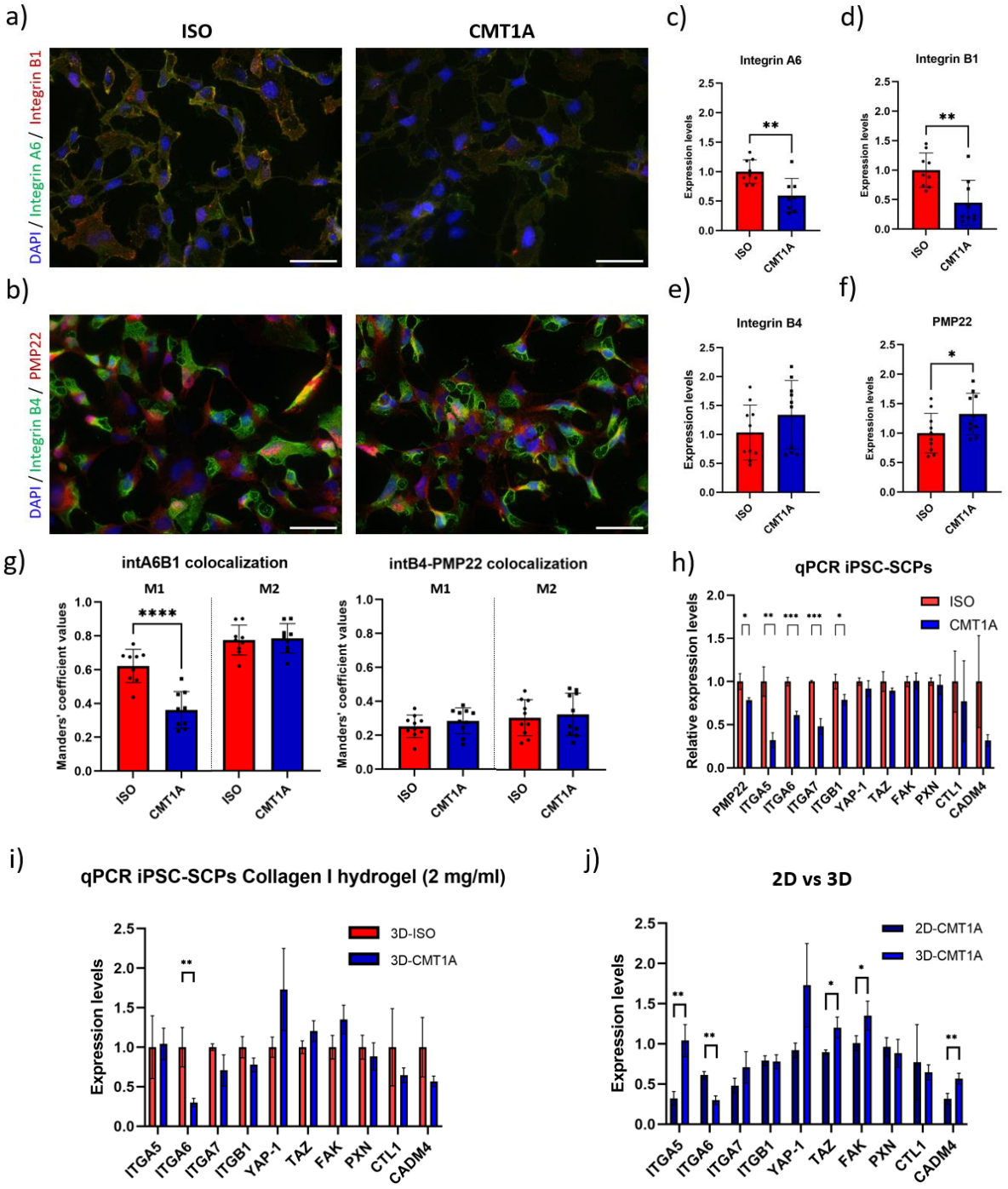

Figure 1 – **CMT1A iPSC-SCPs have an overall decreased integrin expression profile.** a-b) Representative images of immunocytochemical staining of integrin α6 (green), integrin β1 (red), integrin β4 (green) and PMP22 (red), combined with DAPI-counterstaining (blue) in CMT1A and ISO SCPs from n=1 patient. Scale bar: 50 µm. c-f) n= minimum of 327 cells/group (c-d) and 404 cells/group (e-f), 1 experimental repeat. Integrated density was measured, normalized and compared between ISO and CMT1A groups. g) Manders' coefficient analysis on the colocalization of (1) integrin α6 and integrin β1 and (2) integrin β4 and PMP22. Image pixel intensity thresholds of (c-f) were used in (g). h-j) qPCR analysis on targets relating to the cell-ECM axis in SCPs cultured in 2D (h; n=3) and 3D (i; n=2-3). Comparison of expression levels in 2D versus 3D environment (j). P-values: *p<0.05; **p<0.01; ***p<0.001; ****p<0.0001. Unpaired two-tailed t-test (c,e,f,h,i) or Mann-Whitney U test (d,g) was used. Data are presented as mean ± SD.

GP-values (GP > 0.4) (Supplementary Fig. 2d). Finally, MANOVA analysis on phasor plot data populations indicates a very strong significant effect of ISO/CMT1A grouping on the data distribution (Supplementary Fig. 2e). Overall, the Di-4-ANEPPDHQ and Laurdan GPMV datasets suggest that CMT1A SCPs have altered a lower membrane lipid generalized polarization and distinct membrane spectral properties.

Spatiotemporal tracking with Ctxb highlights increased lipid raft presence and decreased dynamics in CMT1A iPSC-SCPs. - To determine the overall presence of lipid rafts, and potential integration of PMP22 within these rafts, we did multiple Ctxb-AF488 labelling experiments on iPSC-SCPs. GM1 labelling with Ctxb-AF488 combined with a PMP22 staining (abcam) reveals significantly lower PMP22 and higher ganglioside GM1 levels in CMT1A SCPs vs isogenic controls

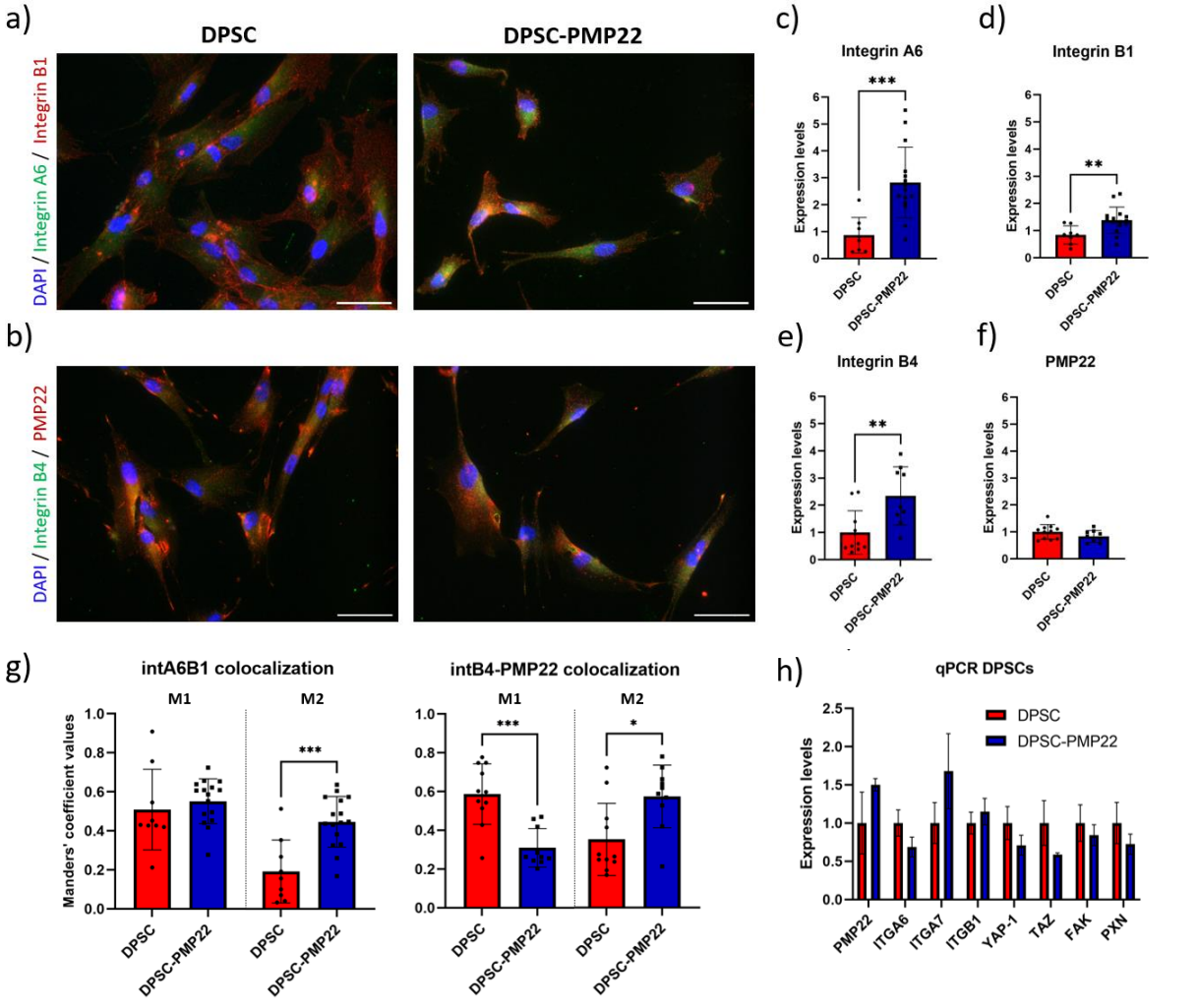

Figure 3 – **PMP22 overexpressing DPSCs display increased expression of integrin α6, β1 and β4.** a-b) Representative images of immunohistochemical staining of Integrin α6 (green), Integrin β1 (red), Integrin β4 (green) and PMP22 (red), combined with DAPI-counterstaining (blue) in DPSCs and DPSC-PMP22s from n=1 patient. Scale bar: 50 µm. c-f) 1 experimental repeat, n= minimum of 124 cells/group (c-d) and 96 cells/group (e-f). Integrated density was measured, normalized and compared between control DPSC and DPSC-PMP22 groups. g) Manders' coefficient analysis on the colocalization of (1) integrin α6 and integrin β1 and (2) integrin β4 and PMP22. Image pixel instensity thresholds of (c-f) were used in (g). h) qPCR analysis on targets involved in integrin-ECM coupling (n=3). P-values: *p-value < 0.05; **p-value < 0.01; ***p-value < 0.001. Unpaired two-tailed t-test (c,d,e,f,g-[intA6B1]) or Mann-Whitney U test (g-[intB4-PMP22], was used. Data presented as mean ± SD.

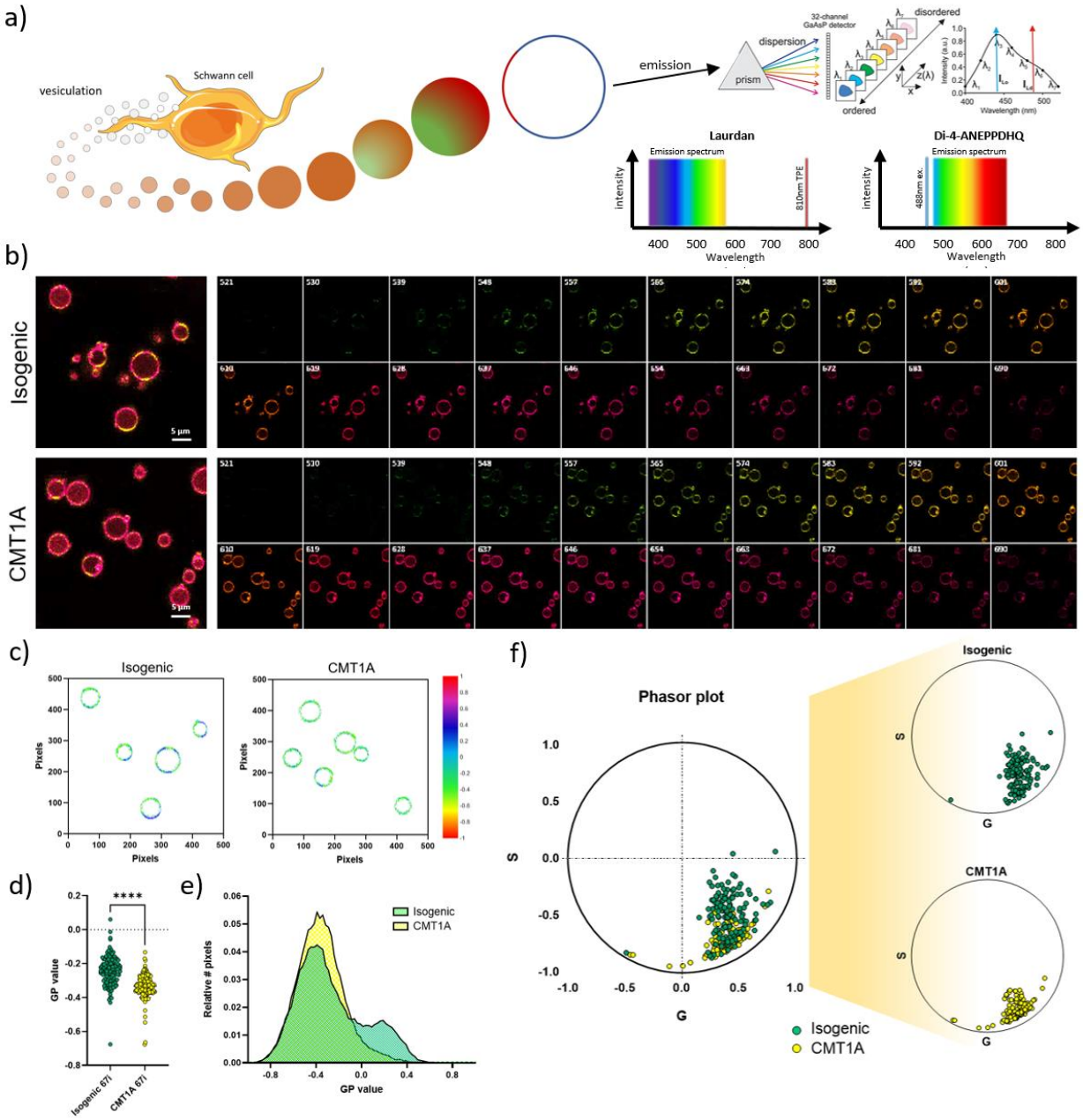

Figure 4 – **Spectral imaging of GPMVs with Di-4-ANEPPDHQ reveals a decrease in CMT1A iPSC-SCP cell membrane ordering.** a) Overview graphic of GPMV synthesis and spectral imaging. By inducing vesiculation, GPMV isolation and membrane staining with Di-4-ANEPPDHQ (see methods), subsequent spectral imaging provides insight in membrane polarization. b) Representative images of ISO and CMT1A SCP GPMVs at different wavelengths (521-690nm; 9nm interval). c) GP value per pixel in ISO and CMT1A SCP GPMVs. d) Quantitative GP value comparison of ISO and CMT1A SCPs. Mann-Whitney U test; P-value: ****p<0.0001. e) Representative processed images (GP-value) of isogenic and CMT1A SCP GPMVs. f) Phasor plot distribution of isogenic and CMT1A SCP GPMV emission spectra. MANOVA analysis provides insight into the large effect of the ISO-CMT1A grouping on the data distribution (p-value <0.0001; Partial Eta Squared = 0.35).

(Fig. 5a-c). Analysis of the PMP22-ganglioside GM1 expression levels reveals a tendency towards an inverse correlation, but non-significant in nature (r= -0.5611; p= 0.116) (Fig. 5d). The Manders' colocalization coefficient of PMP22 with Ganglioside GM1 is significantly increased (~3x increase), but ganglioside GM1 does not colocalize differently with PMP22 in CMT1A SCPs (Fig. 5e).

Ganglioside GM1 is normally enzymatically processed by beta-galactosidase-1 into ganglioside GM2, therefore we analyzed the mRNA levels of GLB1 both in 2D- and 3D-cultured SCPs. A trend towards decreased mRNA expression of GLB1 was found in 2D (p-value: 0.1), and a significant decrease in GLB1 was present in 3D (Fig. 5f). In a TIRF live cell imaging experiment on lipid raft dynamics overtime, a significant difference was found in the mean square displacement of the Ctxb labeled rafts (Fig. 5g-i). Additionally, the mobile/immobile fraction was also significantly different in CMT1A, where the fraction immobile particles was increased. Conclusively, these data indicate there are differences in lipid raft presence and dynamics in CMT1A SCPs, and particularly in the context of ganglioside GM1 (a well-studied lipid-raft component).

CMT1A iPSC-SCPs differ in their lipid contents, as well as their phospholipid and cholesterol metabolism. - RNA sequencing analysis of the major phospholipid biosynthetic pathways (Kennedy pathway [CDP-choline and CDP-ethanolamine pathways], phosphatidylserine (PS) synthase pathway, PS decarboxylase pathway) and membrane incorporating molecules (ORP5, ORP8, PCTP) highlights major disturbances in CMT1A SCPs, compared to their isogenic counterpart (Fig. 6a). Most notably, rate-limiting enzymes CCTa, CCTb and CPT are most heavily altered in CMT1A, highlighting a likely key contribution of Kennedy pathway disturbances in CMT1A. Mass spectrometry quantification of lipid species in CMT1A and isogenic SCPs further supports a phospholipid-cholesterol disturbance aspect in the disease pathology since cholesterol, phosphatidylcholine, phosphatidylethanolamine, phosphatidylinositol and phosphatidylserine are decreased in abundance, along with ceramide and diacylglycerol (Fig. 6b). Furthermore, we did an Amplex Red™ cholesterol assay to provide preliminary insights into total cholesterol, free cholesterol and esterified cholesterol levels. Here, we see a clear trend that CMT1A SCPs have lower cholesterol contents of all forms mentioned above (Fig. 6c). By measuring both the medium and cellular cholesterol content (representing released and cellular cholesterol, respectively) after a period of 4 hours on new culture medium (with or without ApoA1), we found a significantly higher efflux rate in CMT1A without ApoA1 (Fig. 6d). However, when ApoA1 was supplemented, the efflux rates of both groups reached a similar level (~12%) (Fig. 6d). Since ApoA1 improves the efflux of cholesterol and phospholipids through ABCA1, we next determined ABCA1 mRNA expression levels in our SCP model (Fig. 6e). ABCA1 transcripts were strongly decreased, providing an explanation for the difference in efflux with and without ApoA1 supplementation. Next, the efficiency of myelin uptake by SCPs was determined by adding DiI-labeled human CNS myelin for 90 min and subsequent FACS analysis to quantify to amount of uptake. A trend towards more uptake, but no significant increase is seen in CMT1A SCPs compared to ISO controls. Finally, we investigated how SCPs from CMT1A patients (vs ISO controls) can deal with changes in their lipid milieu and how this affects their membrane spectral properties. Therefore, SCPs were cultured in medium supplemented with either milliQ (control), 1 µM choline-chloride, 1µM methyl-β-cyclodextrin (MBCD; depletes cholesterol) or 100 µg/ml human CNS myelin, and afterwards GPMVs were formed and labelled with Di-4-ANEPPDHQ as described above to determine membrane polarity. For both isogenic and CMT1A SCPs we found that the GP-values of the control, choline chloride and myelin groups were significantly higher than the MBCD treated group. However, no differences were observed between the other groups (Fig. 6g). Additionally, control and MBCD conditions of the CMT1A SCP group have a significantly higher and lower GP-value than their isogenic counterpart, respectively (Fig. 6h). By using phasor plots to analyse the GPMV spectral data distribution, data populations can be compared (presented as probability ellipses with p=0.9). Different stimulating conditions used provide different population ellipses. Overlap between stimulation groups versus the control group is visibly still high, except for the MBCD group which has minimal overlap both in isogenic and CMT1A phasor plots. However, the different conditions do have a strong significant effect on the phasor plot data distribution (Fig. 6i). Furthermore, within conditions there are minor data population shifts visible between isogenic and CMT1A groups, especially

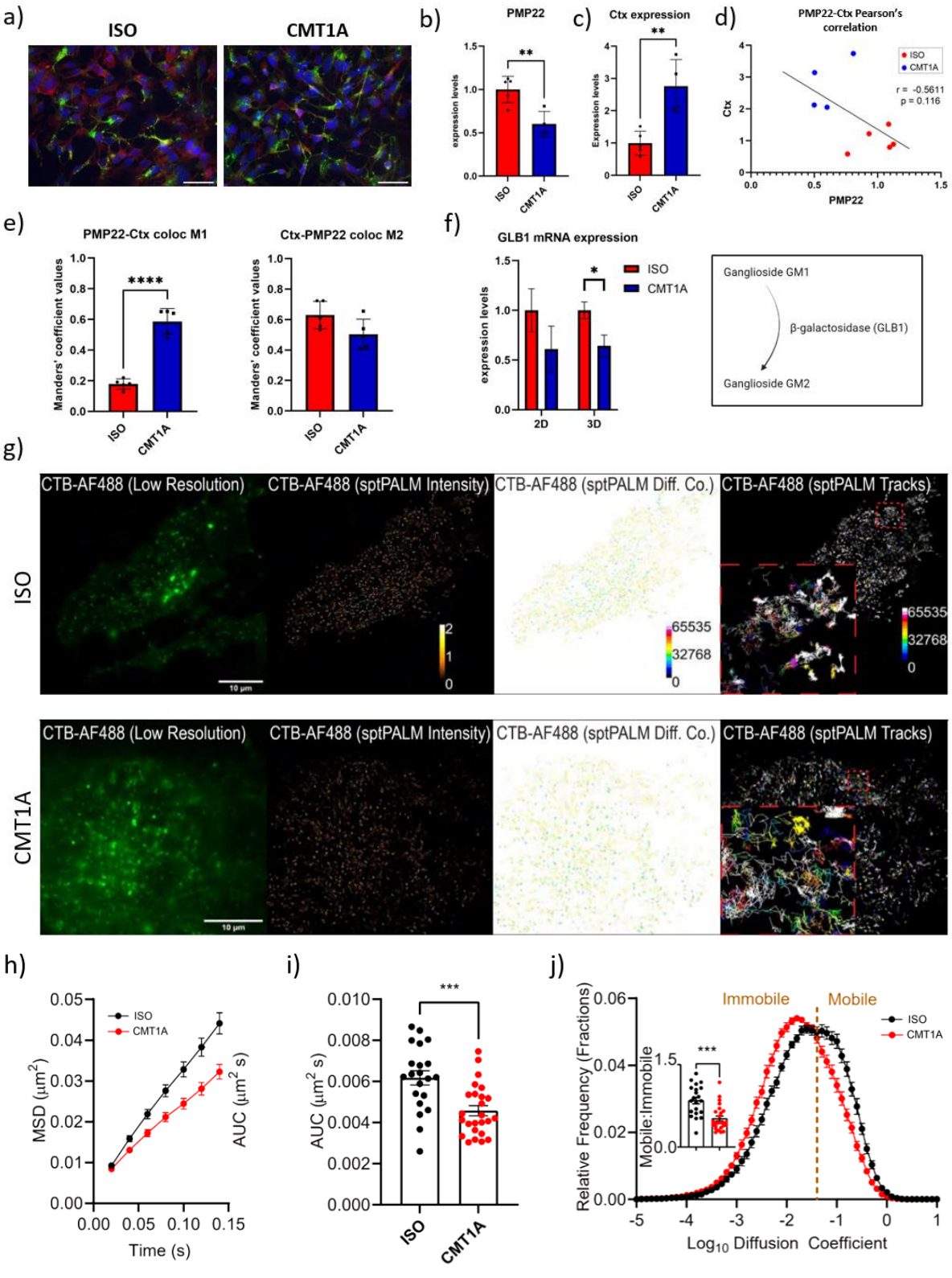
a)
ISO
CMT1A
b)
PMP22
expression levels
**
ISO
CMT1A
c)
Ctx expression
Expression levels
**
ISO
CMT1A
d)
PMP22-Ctx Pearson's correlation
ISO
CMT1A
r = -0.5611
p = 0.116
Ctx
PMP22
e)
PMP22-Ctx coloc M1
Manders' coefficient values
****
ISO
CMT1A
Ctx-PMP22 coloc M2
Manders' coefficient values
ISO
CMT1A
f)
GLB1 mRNA expression
expression levels
*
ISO
CMT1A
2D
3D
Ganglioside GM1
β-galactosidase (GLB1)
Ganglioside GM2
g)
ISO
CTB-AF488 (Low Resolution)
CTB-AF488 (sptPALM Intensity)
CTB-AF488 (sptPALM Diff. Co.)
CTB-AF488 (sptPALM Tracks)
65535
32768
0
10 µm
CMT1A
CTB-AF488 (Low Resolution)
CTB-AF488 (sptPALM Intensity)
CTB-AF488 (sptPALM Diff. Co.)
CTB-AF488 (sptPALM Tracks)
10 µm
h)
ISO
CMT1A
MSD (µm²)
AUC (µm² s)
Time (s)
i)
***
AUC (µm² s)
ISO
CMT1A
j)
Immobile
Mobile
ISO
CMT1A
Relative Frequency (Fractions)
Mobile:Immobile
***
Log10 Diffusion Coefficient

Figure 5 – **Lipid rafts in the cell membrane of CMT1A iPSC-SCPs are less mobile than these of isogenic controls.** a) Representative images of immunocytochemical staining of PMP22 (red) combined with a Ctxb-AF488 (green) GM1 ganglioside labelling (lipid raft) in SCPs. Scale bar: 50 µm. b-c) n= minimum of 295 cells/group, 1 experimental repeat. Integrated density was measured, normalized and compared between ISO and CMT1A groups. d) Pearson's correlation analysis of PMP22 and Ctx expression levels. e) Manders' coefficient analysis on the colocalization of PMP22 and Ctx. f) GLB1 mRNA expression in 2D and 3D cultured SCPs. g) Representative TIRF-microscopy images (left-right: raw image Ctxb-labelling, intensity map, diffusion coefficient map and trajectory map) of live-cell lipid raft labelling of ISO and CMT1A SCPs (1 frame/0.033s; 1000 frames). Scale bar: 10 µm h-i) Average mean square displacement of SCPs over 150 µs. j) Ratio fraction of mobile:immobile rafts of ISO and CMT1A SCPs. P-values: *p<0.05; **p<0.01; ***p<0.001; ****p<0.0001. Ctx = Cholera toxin; GLB1 = β-galactosidase. Data are presented as mean ± SD.

in the myelin group where the data distribution is relatively very little compared to CMT1A (Fig. 6j).

Lipid droplet formation is altered in CMT1A iPSC-SCPs, and this effect can be reversed by stimulating the PPARg-LXR-ABCA1 axis. **-** We used a BODIPY™ labelling on cultured SCPs to determine the amount of cytoplasmic (neutral) lipid droplets. Isogenic and CMT1A SCPs were cultured with myelin, myelin + Rosiglitazone (PPARg agonist) or myelin + T0901317 (LXR agonist), and afterwards the integrated densities of the BODIPY™ labelled lipids was quantified (Fig. 7a). Interestingly, myelin supplementation leads to a significant increase in the amount of neutral lipids in isogenic SCPs, while this effect was less strong in CMT1A cells (Fig. 7b). By adding Rosiglitazone and T0901317 to these myelin conditions we found that the amount of neutral lipids was significantly decreased in isogenic SCPs. In addition, T0901317 supplementation lead to an increase in neutral lipid content in CMT1A SCPs compared to the other stimulation conditions. Additionally, a FACS experiment provides further insights into the decreasing trend in neutral lipids seen in CMT1A SCPs (Fig. 7c) compared to isogenic controls. Since lipid droplet formation is regulated by Seipin (*BSCL2*-gene), we performed qPCR and found that was significantly increased in 2D, but no difference was detected in cells cultured in 3D (Fig. 7d).

CMT1A iPSC-SCPs display no macroscopic and microscopic contraction differences in collagen I hydrogels, but have a reduced migration rate versus isogenic controls. **–** Cells were cultured in a 3D-endoneurium-like free-floating collagen I hydrogel (as described in methods) to examine contraction both macro- and microscopically. Macroscopic contraction was examined at multiple timepoints, and phase-contrast images were made to provide insights in cell morphology development over time (Fig. 8a). At these timepoints, macroscopic images were made of the hydrogels and their area was measured and compared over time (Fig. 8b). No significant differences were detected at different timepoints after 48 hours (Fig. 8c), and also not after 96h which was verified in a follow-up experiment (Fig. 8d). Microscopic SHG-autofluorescence images of the hydrogels used in Figure 8a-c also reveal that there are no contractile changes and no alterations in collagen fibre alignment between isogenic and CMT1A SCPs (Fig. 8e,f). Since Schwann cell precursors have distal migration as a main feature during peripheral nerve development, we next did a scratch assay and we analyzed migration in a time frame of 64h (Fig. 8g). Wound confluence was significantly lower in CMT1A SCPs, indicating that their migratory capacity is reduced compared to isogenic SCPs (Fig. 8h). Overall these results do not provide any evidence for cell-ECM interaction changes between SCPs and an endoneurial environment, but do reveal altered migration capacity in CMT1A SCPs.

DISCUSSION

The aim of this study was to further specify the changes in CMT1A Schwann cell membranes, mainly concerning integrin receptors, cell (membrane) lipid properties and metabolism, and cell-ECM dynamics. Previous studies have provided evidence for disturbances in the membrane integrin receptor and cellular lipid profile in the case of *PMP22* deletion in Schwann cell models (39, 40, 52). However, in this study we describe their alteration for a first time in human CMT1A *in vitro* models (i.e. PMP22-overexpressing Schwann cell models).

In our CMT1A iPSC-SCP model, we see an unexpected decrease in *PMP22* mRNA levels despite having an extra copy of the *PMP22*-gene. In spite of that, via immunocytochemistry analysis

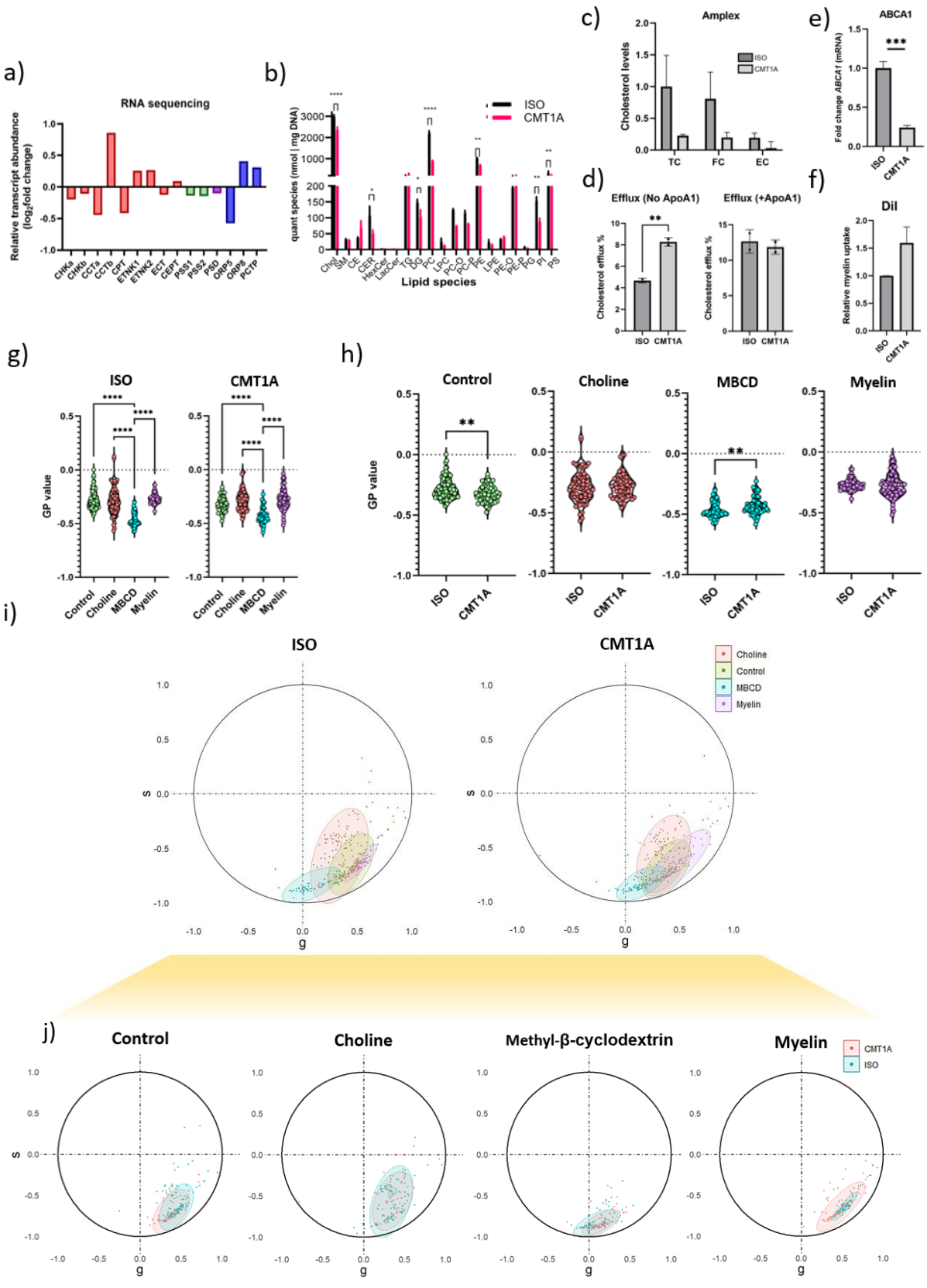
a)
RNA sequencing
Relative transcript abundance (log2fold change)
CHKa CHKb CCTa CCTb CPT ETNK1 ETNK2 ECT CEPT PSS1 PSS2 PSD ORP5 ORP8 PCTP
b)
ISO
CMT1A
quant species (nmol | mg DNA)
Chol SM CE CER HexCer LacCer TG DG PC LPC PC-O PC-P PE LPE PE-O PE-P PG PI PS
Lipid species
c)
Amplex
Cholesterol levels
TC FC EC
e)
ABCA1
Fold change ABCA1 (mRNA)
d)
Efflux (No ApoA1)
Efflux (+ApoA1)
Cholesterol efflux %
f)
DiI
Relative myelin uptake
g)
ISO
CMT1A
GP value
Control Choline MBCD Myelin
h)
Control
Choline
MBCD
Myelin
i)
ISO
CMT1A
Choline
Control
MBCD
Myelin
s
g
j)
Control
Choline
Methyl-β-cyclodextrin
Myelin
CMT1A
ISO

Figure 6 – **Lipidomic analysis indicate disturbed lipid metabolism and cell membrane profile in CMT1A SCPs.** a) RNA sequencing analysis in iPSC-SCPs of enzymes in the CDP-choline and –ethanolamine pathway (red), PS-biosynthesis pathway (green), PSD-pathway (purple) and phospholipid membrane incorporation mechanism (blue). All enzyme expression levels presented are significantly different between ISO and CMT1A iPSC-SCP groups. b) Mass spectrometry lipid abundance analysis in ISO and CMT1A iPSC-SCPs. c) cholesterol fluorescence levels of myelin-treated ISO vs CMT1A iPSC-SCPs, measured through an Amplex cholesterol assay. Cholesterol levels are normalized to the ISO TC group (n=2). d) Cholesterol efflux of non-myelin treated iPSC-SCPs over 4h, expressed in % of total cholesterol measured (n=2). e) qPCR analysis of ABCA1 expression (n=3; p-value: 0.0002). f) DiI-labelled myelin uptake assay in ISO and CMT1A iPSC-SCPs. Uptake was quantified after 90 minutes through FACS. g) ISO and CMT1A GPMV generalized polarization (GP)-values of control, choline-chloride, Methyl-ß-cyclodextrin (MBCD) and myelin groups. h) comparison per condition of the GP-values presented in (g) between ISO and CMT1A GPMVs. i) Phasor plot distribution of ISO and CMT1A iPSC-SCP GPMV Di-4-ANEPPDHQ emission spectra of the different conditions. MANOVA analysis indicates significant contribution of stimulation conditions on the data distribution (ISO: p-value = <0.0001; Partial Eta Squared = 0.33; CMT1A: p-value = <0.0001; Partial Eta Squared = 0.26). j) Phasor plot distribution of ISO vs CMT1A GPMVs for every condition mentioned in (i). MANOVA test reveals medium-sized significant effects on data distribution differences seen between ISO and CMT1A in the control (p-value = 0.02682; Partial Eta Squared = 0.04) and myelin groups (p-value = 0.0006; Partial Eta Squared = 0.1). Data distribution in (i) and (j) is presented by means of a probability-ellipse (p=0.90) to highlight the data distribution per condition. P-values: *p<0.05, **p<0.01, ****p<0.0001. Unpaired two-tailed t-test (d), Mann-Whitney U test (h) and multiple t-test (g) was used. Data are presented as mean ± SD. ETNK = ethanolamine kinase; CHK = choline kinase; ECT = CTP:phosphoethanolamine cytidylyltransferase; CCT = CTP:phosphocholine cytidylyltransferase; CEPT = choline/ethanolaminephosphotransferase; CPT = choline phosphotransferase; PSS1/2 = phosphatidylserine synthase 1/2; ORP5 = oxysterol-binding protein-related protein 5; ORP8 = oxysterol-binding protein-related protein 8; PCTP = phosphatidylcholine transfer protein; Chol = Cholesterol; SM = Sphingomyelin; CE = Cholesterol ester; CER = Ceramide; HexCER = Hexosyl ceramide; LacCER = Lactosyl ceramide; TG = Triglyceride; DG = Diacylglycerol; LPC = Lysophosphatidylcholine; PC-O = oxidized phosphatidylcholine; PC-P = phosphorylated phosphatidylcholine; PE-O = oxidized phosphatidylethanolamine; PE-P = phosphorylated phosphatidylethanolamine; PG = phosphatidylglycerol; PI = phosphatidylinositol; PS = phosphatidylserine

we did observe an increase in PMP22 protein expression in CMT1A SCPs. It is well known that several factors may influence PMP22 protein and mRNA levels, such as integrin β4 and ABCA1 expression levels. Additionally, only 20% of *PMP22* transcripts eventually form PMP22 proteins. These factors all provide layers of complexity towards PMP22 data interpretation and CMT1A translation (19, 21, 53). Previously, it was shown that integrin β4 protein levels are decreased in $PMP22^{-/-}$-mice during development and maturation (14, 32, 52, 54). Interestingly, integrin β4 ablation appeared to increase protein levels of PMP22, but not mRNA levels (53). Integrin β1 levels on the contrary were found to remain elevated during maturation, compared to healthy control nerves (52). In our iPSC-SCP model, we see an overall decrease in both mRNA and protein levels of integrin α6 and β1 and a decrease in integrin α5 and α7 mRNA levels. However, we did not see integrin β4 protein level differences in 2D SCPs despite a small trend towards an increased expression. Furthermore, expression patterns of these integrins remained similar in isogenic and CMT1A SCPs, since they were generally expressed in the cell membrane. However, a distinct expression pattern is seen for integrin β4, which was mainly located at cell processes. Colocalization in 2D-cultured SCPs also reveals a decrease in colocalization of integrin α6 with integrin β1, potentially explaining a decrease in functional ECM interaction in CMT1A Schwann cells. However, no integrin expression differences (except for a decrease in integrin α6) were seen in 3D-cultured CMT1A SCPs compared to controls. SCPs are mainly migratory in nature, which depends on axonal and ECM signals, and only contribute to PNS embryological development (55). Therefore, the 3D collagen I environment does not provide the true SCP environment and in situ cell-ECM interactions (30, 56). These findings translate to a general decrease in interaction with basal lamina and ECM components in CMT1A SCPs. In conclusion, our CMT1A SCP model reveals expression patterns of integrins that are in line with previous findings in *PMP22*-knockout (*PMP22*-KO) models (14, 36, 52).

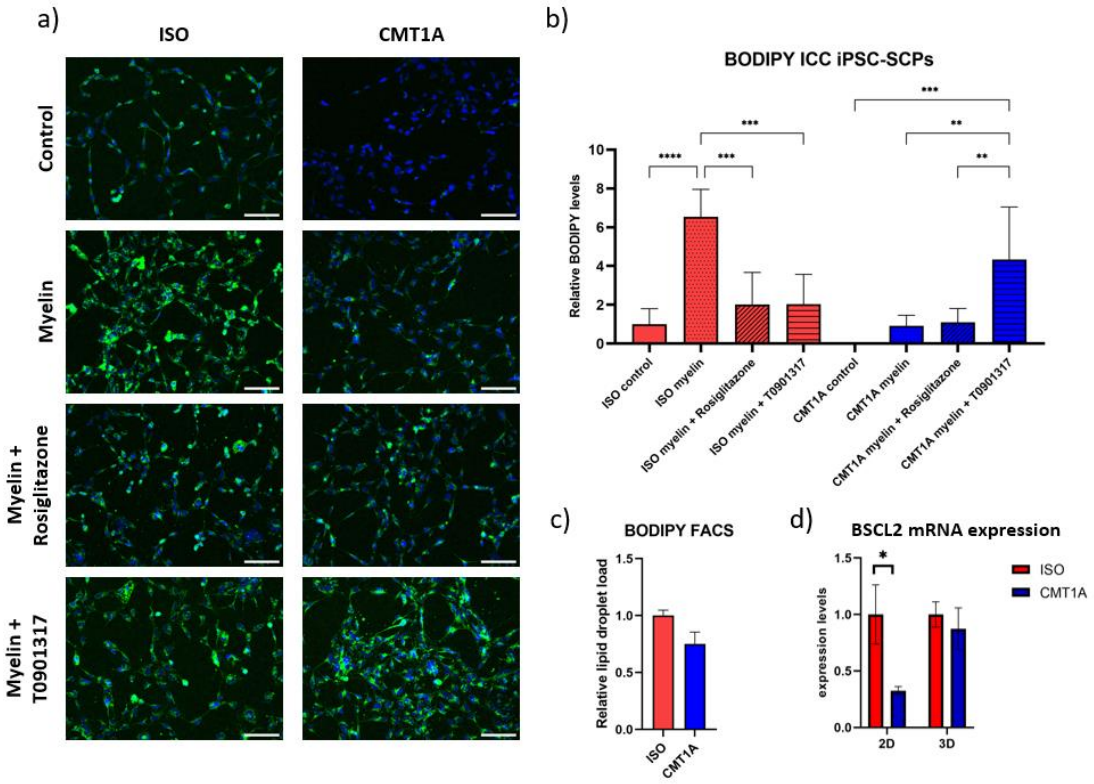

Figure 7 – **Stimulation with myelin increased lipid droplet content in isogenic and CMT1A iPSC-SCPs but can be restored through stimulation of the LXR/PPARg axis.** a) BODIPY labelling (green) of SCPs after stimulation with myelin, myelin + rosiglitazone, or myelin + T0901317 for 24h. Cells were counterstained for DAPI (blue). Scale bar: 100µm. b) n= minimum of 875 cells/group, 1 experimental repeat. Integrated density was measured, normalized and compared between ISO and CMT1A groups. c) BODIPY-FACS quantification of myelin-treated ISO and CMT1A SCPs (n=2). d) qPCR analysis of BSCL2 expression in SCPs in 2D- and 3D-culturing conditions (n=3). P-values: *p<0.05; **p<0.01; ***p<0.001; ****p<0.0001. Data are presented as mean ± SD.

We also used DPSCs as an additional model to investigate the effects of an increase in *PMP22*-gene copy number. DPSCs are a neural crest-derived stem cell population located in tooth pulp. Recently, it has been shown in mice that they originate from Schwann cell precursors that populate the tooth during development/innervation (57). Therefore, induction of extra *PMP22* genetic copies in DPSCs provide a CMT1A Schwann cell-like model for further analyses. Interestingly, we found contradicting results using these PMP22 overexpressing DPSCs compared to the iPSC-SCP model. A trend towards an increased mRNA expression, but no differences in protein expression is seen in DPSC-PMP22s. Integrin α6, β1 and β4 expression levels are strongly increased based on immunocytochemistry analyses of DPSC-PMP22s compared to control DPSC lines. Their expression patterns are also distinct from those in SCPs: integrin α6 is expressed within the cell membranes, while integrin β1 and β4 are expressed in a more diffuse pattern in the DPSC cell body cytoplasm. Additionally, in immunocytochemistry stainings, integrin β1 was more colocalized with integrin α6. Furthermore, integrin β4 colocalized less with PMP22, but PMP22 colocalized significantly more with integrin β4, possibly due to the increase in integrin β4 protein levels. Possible explanations for the discrepancies seen in both our models are that the PMP22-induction has resulted in only a minor overall increase in PMP22 in the total DPSC population, compared to the PMP22-duplication in the whole CMT1A iPSC-SCP population. Laminin coating in SCP cultures may also cause the decrease in integrin α6 (and other integrin) expression levels (58). Additionally, DPSCs are neural crest-derived, but different from Schwann cells by further differentiating locally during development and the tooth microenvironment (57, 59).

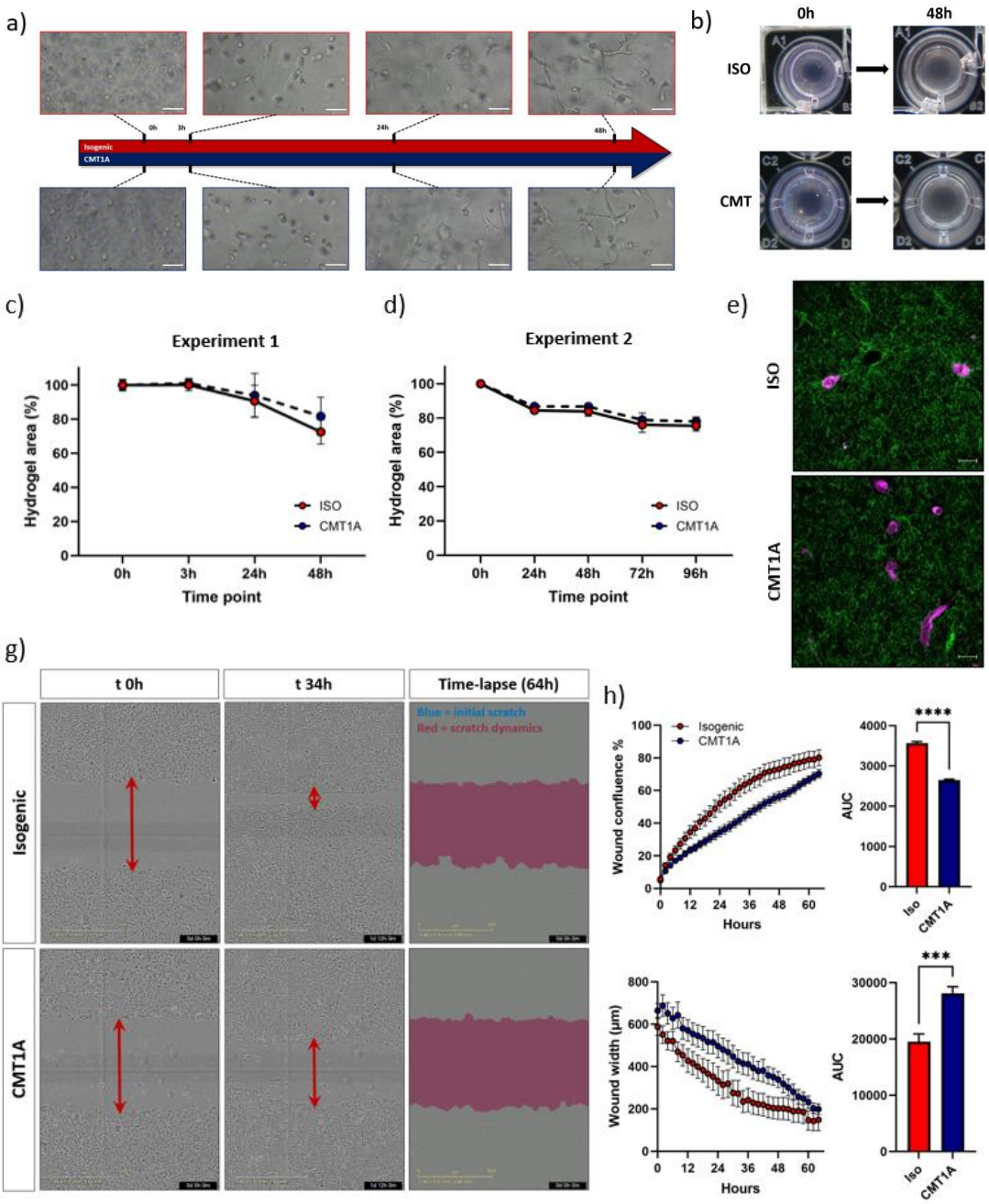

Figure 8 – **CMT1A iPSC-SCPs show no macro- or microscopic contractile changes, but do have a reduced migratory rate.** a) Timeline depicting the temporospatial cell morphology development of isogenic and CMT1A SCPs in a collagen I hydrogel matrix (2 mg/ml). Scale bar: 50 µm b) representative macroscopic images at 0h and 48h post cell-embedment. c) Macroscopic contraction experiment, performed by hydrogel surface area measurement at multiple timepoints (0, 3, 24 and 48 hours). Data is presented as mean ± SD. No strong area decrease was observed and there was no significant difference between ISO and CMT1A cells (two-way ANOVA with Bonferroni post hoc test). d) macroscopic contraction experiment (c) with a longer follow up period (96h), highlighting the similar small area decrease pattern in ISO and CMT1A cell-embedded collagen I hydrogels. e) Representative SHG (collagen fibrils, green) and autofluorescence (cell bodies, purple) microscopic images of ISO and CMT1A cells in a collagen I hydrogel (2 mg/ml). Scale bar: 20 µm. f) images from a scratch assay Incucyte time-lapse in isogenic and CMT1A cell cultures over 64 hours. g) wound healing analysis of the Incucyte experiment described in (f). Data are presented as mean ± SEM. Wound confluence was higher and wound width was smaller in the isogenic cell group. *** $p<0.001$; **** $p<0.0001$.

Recent studies have also provided evidence that SCPs are highly multipotent. This is evident in the many functions of SCPs outside of PNS development and makes SCPs very similar to NCCs, possibly limiting the accuracy of our iPSC-SCP model for correct interpretations regarding the PMP22-myelin axis in CMT1A (60). However, zPMP22 (zebrafish orthologue of PMP22) has been linked to the correct differentiation and migration of NCCs in *Brachydanio rerio* (zebrafish), and PMP22 has been detected in neural crest stem cells from dorsal root ganglia (DRG) and in iPSC-NCCs, where it increases cellular oxidative stress levels (61, 62). Overall, despite mentioned limitations, the evidence supports the use of our iPSC-SCP model as a model for CMT1A research and makes it currently preferable over PMP22 overexpressing DPSC. Ideally, in the near future, DPSCs of CMT1A patients will be used to accurately represent their chromosome 17p11.2 duplication. However, further research is needed for accurate CMT1A Schwann cell model formation. Ideally, this will be done using immature or myelinating Schwann cells in a 3D endoneurium-like environment.

Since cell membrane receptors and transmembrane proteins depend on a stable cell membrane, we explored cell membrane lipid properties in CMT1A SCPs using the GPMV model, Ctxb lipid raft labelling and phospholipid/cholesterol metabolism interventions in combination with. Both Di-4-ANEPPDHQ and Laurdan labelling highlights decreases in GP values and large shifts in spectral phasor plots of CMT1A vs isogenic SCP GPMVs. Lower GP values correlate usually with an increase in membrane fluidity and polarity, and a more disordered overall membrane lipid structure. Additionally, lower GP values correlate with lower cholesterol and saturated fatty acid content levels in the cell membrane (63, 64). Laurdan GP value shifts are strongly correlated with dipolar relaxation, generally depending on the degree of lipid packing and thus a sensitive proxy for lipid order. Di-4-ANEPPDHQ labelling, however, does not correlate with lipid packing. The emission of this environmental sensitive dye is influenced primarily by membrane cholesterol content levels. Altogether, GPMV results from this study reveal that cell membranes of CMT1A SCPs are less tightly packed and have a decreased cholesterol content. The latter is possibly manifested via perturbed cholesterol incorporation in the cell membrane due to PMP22 expression changes, since this has been described prior in PMP22-KO Schwann cells (20). After stimulation of SCPs with choline chloride (which stimulates the CDP-choline branch of the Kennedy pathway, see above), methyl-β-cyclodextrine (depletes cholesterol, see above) and human CNS myelin, only a decrease in GP value is seen in the methyl-β-cyclodextrine groups versus the other groups, likely due to the free cholesterol ablating effect of Di-4 which was used for spectral imaging in this experiment (65, 66). However, the overall effect of the stimulating agents on membrane polarity indicates that interventions in the phospholipid/cholesterol metabolism can possibly restore the CMT1A membrane polarity towards the membrane polarity of the isogenic controls. However, in order to do this, better understanding of the specific metabolism changes underlying the CMT1A pathobiology is needed.

Another essential component — and indispensable for proper membrane receptor functionality — are lipid rafts in the cell membrane because a lot of receptor signaling processes are regulated in these nanodomains (67). PMP22 has been localized previously in lipid raft structures. Additionally, in sciatic nerves, PMP22-KO leads to altered localization of Flotillin-1 (a raft component) (20). In this study, we used Ctxb (which binds GM1 ganglioside) to visualize and track lipid rafts in the plasma membrane of SCPs. Our results highlight that there is a lower degree of raft mobility in CMT1A. This will possibly lead to a decreased mobility of raft-associated integrins, which is needed to maintain a correct dynamic interaction with the microenvironment (68). Interestingly, an overall increase in ganglioside GM1/lipid rafts was found in CMT1A SCPs together with a decrease in transcript levels of the ganglioside GM1 converting enzyme, GLB1. In this experiment, we did find lower PMP22 protein levels (contrary to the previously described ICC experiment). A possible explanation is that we used a different PMP22 antibody in this particular experiment. However future Western blot experiments are recommended to further determine what happens exactly with PMP22 expression at the proteomic level. Nevertheless, PMP22 levels did seem to provide an inverse correlation trend with GM1 ganglioside

levels, and PMP22 was strongly increased in its colocalization with ganglioside GM1 in CMT1A SCPs. Altogether, we conclude that further PMP22 expression experiments are essential in the iPSC-SCP model described here, but that lipid raft disturbances are a major aspect of the lipidomic distortions thus far described in PMP22-deficient and overexpressing models.

In previous studies, lipid quantity alterations have been described in CMT1A rat models. Previously detected phospholipid quantity alterations were large; PC and PS were proportionally more abundant with saturated fatty acid chains compared to unsaturated fatty acid chains, and PE was increased in CMT1A rat Schwann cells (40). However, no overall phospholipid/cholesterol abundance analysis has thus far — to the best of our knowledge — been done on CMT1A Schwann cell models. Our mass spectrometry analysis on cellular lipid quantities reveals an overall decrease in cholesterol, ceramides, diacylglycerides, PC, PE, oxidized PE, PI and PS in CMT1A SCPs. Additionally, in line with previous discoveries of decreased cholesterol efflux rates to ApoA-I PMP22-KO mouse Schwann cells, we found that overall the efflux of cholesterol was increased without ApoA-I, but not with ApoA-I in CMT1A SCPs compared to isogenic controls. Complementary to the efflux analysis, we have seen a strong trend towards a decrease in both free and esterified cholesterol content, a strong reduction in ABCA1 mRNA transcript levels and a trend towards an increased DiI-myelin uptake for the CMT1A group. These findings are interesting, since one of the main cholesterol efflux route is mediated through ABCA1 (65, 69). Possibly, the decrease in ABCA1 mRNA expression underlies the relative increase in efflux seen after ApoA-I supplementation. Additionally, the increased efflux seen in CMT1A Schwann cells provides an explanation for the decreasing trend in cholesterol content seen, even though there seems to be an increased overall myelin/lipid uptake in CMT1A SCPs versus isogenic controls. A couple of studies have already described general transcriptomic alterations in CMT1A regarding lipid metabolism. Generally, lipid metabolism pathways were among the most severely dysregulated at the transcriptomic level in CMT1A rat Schwann cells and DRGs (37, 39). More specifically, in CMT1A rats the phospholipid, cholesterol and glycosphingolipid biosynthesis were downregulated. Most notably, the phosphatidylcholine metabolism appeared most impaired, similar to what is seen in our RNA sequencing data. Interestingly, despite reduced absolute quantities of PE, we see an overall increase in the rate-limiting enzyme expression in the CDP-ethanolamine branch of the Kennedy pathway (*ETNK1*, *ETNK2*) on the mRNA level. It has previously been established that both cholesterol and PE both increase the rigidity of the cell membrane and that cholesterol decreases are compensated by PE increases (and vice versa), maintaining the membrane fluidity and overall cell membrane functionality (70). Therefore, the overall lipid ratio's may be altered in CMT1A, providing the polarity alterations seen in the GPMV experiments. However, membrane lipid mass spectrometry analyses on CMT1A models will have to be done in the future to confirm this hypothesis.

In order to maintain the overall cellular lipid homeostasis, lipid droplets are formed. Lipid droplets are cell organelles that are formed in order to store neutral lipids (e.g. triglycerides, sterol esters), separated from the cytoplasm by a phospholipid monolayer (71, 72). By maintaining a reserve for cellular lipid supply, and providing enzymatic support on their membrane, they are important regulators of cellular health and disturbances in neuroglial lipid droplets have been found to contribute to the pathobiology of several neurological disorders (73). Thus far, the role of lipid droplets in Schwann cells has been described in the context of *Mycobacterium leprae* infection, where synthesis of cholesterol, phospholipid and fatty acids is stimulated and leads to more lipid droplet accumulation (74). However, heretofore lipid droplets have not been described in the CMT1A pathobiology. Our results highlight the overall reduced capability of lipid storage with and without myelin/lipid supplementation in CMT1A SCPs. In isogenic SCPs, PPARg or LXR stimulation seems to overcome the increase in lipid droplet formation seen after myelin supplementation. Interestingly, in CMT1A SCPs, LXR agonists lead to an increase in lipid droplet content, but not PPARg stimulation. This contradicts our initial expectation of decreased lipid content via LXR stimulation, since LXRs typically stimulate ABCA1 expression (75). However, LXRs have also been described to influence phospholipid and fatty acid biogenesis, and therefore may induce

the increase in lipid droplets via these mechanisms (76). PPARg generally also promotes lipid storage, but is also a stimulator of LXRα (77, 78). Since PPARg contributes to a multitude of lipid-related pathways, the overall neutral lipid product may therefore be unaltered as is seen in our CMT1A SCPs. Complementary to the BODIPY analysis, we analyzed mRNA levels of *BCL2*, encoding the Seipin protein. Seipin maintain homogeneity in lipid droplet size, regulate the lipid droplet proteome and the lipid droplet-ER interaction, and regulate the cellular lipid homeostasis (79). Seipin-related diseases (commonly referred to as seipinopathies) include CMT2 variants. However, no link has yet been made with CMT1 (80). Our findings illustrate that there is a potential contribution of Seipin towards the CMT1A pathology, but the discrepancy between the 2D and 3D cultured SCPs highlights that the ECM may influence lipid droplet contents. Overall, the results of our BODIPY experiment and BCL2 expression provide a first insight into lipid droplet-associated changes seen in CMT1A in the SCP model.

Finally, general contractile analysis on our iPSC-SCP model revealed an unexpected similarity in isogenic and CMT1A cell-ECM interaction in free-floating collagen I hydrogels. However, SCPs are only dependent on axonal signalling, whereas ECM-signalling starts to become essential only later in the iSC stage of SC development (17, 81). Therefore, these experiments will be repeated at a later stage when iPSC-SCPs have been differentiated into iPSC-iSCs, currently being done by our research group. Additionally, steeper decreases in average diameter seen at 0-24h and 48-72h were possibly caused by a medium change provided every other day (at 0h and 48h in the experiment). Furthermore, temporospatial tracking of SCP migration revealed a decreased migration capacity in these cells. Similarly, a previous study revealed decrease migration in PMP22-KO Schwann cells, but this was rescued by cholesterol supplementation (20). Our findings further contribute to the role of PMP22 in cell migration, an essential aspect of NCCs and SCPs. Since neurocristopathies are generally classified as diseases caused by altered migration or differentiation of NCCs, we additionally provide evidence for a neurocristopathic origin of CMT1A, especially since the distinction between NCCs and SCPs has been up for recent debate (28).

This study is mostly limited in the fact that all experiments were done on iPSC-SCPs and DPSCs of 1 patient each. All experiments should therefore be repeated on multiple patients to confirm the changes seen in this study. Furthermore, more accurate quantification of protein expression levels should done via Western blot experiments and colocalization experiments using STORM super-resolution could provide better insights in colocalization of PMP22 with integrins and lipid rafts. Additionally, differentiation of iPSC-SCPs into (i)SC-like cell types will improve the translatability of these experiments regarding their effect on myelination. Nevertheless, in this study we provide a broad overview of CMT1A changes in integrin receptor expression and colocalization, cellular and membrane lipid proportions and metabolism, and contractile/migratory capacity in our SCP and DPSC model. Our results provide new evidence for similarities between HNPP and CMT1A, and contribute to the increasing body of evidence for a central role of lipid disturbances in CMT1A Schwann cells and their effect on the Schwann cell membrane. Future studies will have to be conducted to map out the exact alterations and to find specific lipid metabolism interventions that can alleviate Schwann cell dysmyelination and the CMT1A clinical phenotype.

CONCLUSION

In this study, we further provide evidence for an overall disturbance in integrin receptor expression profile. Furthermore, we are the first to describe overall changes in the cell membrane lipid profile, specifically in the overall polarity, lipid raft properties, and effect of phospholipid/cholesterol interventions thereon. Adding to the recent evidence of phospholipid and cholesterol disturbances in CMT1A, we confirm these changes in our iPSC-SCP model and provide insights into their lipid droplet content. Finally, we found that migration is altered, but that there are no major cell-ECM interaction distinctions present between CMT1A and control SCPs. Further investigation into the exact integrin receptor expression levels, but also phospholipid and cholesterol biosynthesis alterations are paramount to get a correct understanding of their changes and to ultimately provide interventions for Schwann cell recovery and CMT1A disease alleviation.

Acknowledgements – The authors thank Dr. Robert H. Baloh and Prof. Dr. Ludo Van Den Bosch for developing and providing the iPSC-SCP model and differentiation protocol, Prof. Dr. Martin vandeVen for developing and executing the Matlab protocol to analyze the GPMV and iPSC-SCP collagen I hydrogel SHG data. We are very grateful and acknowledge the Research Foundation Flanders (FWO Vlaanderen) for the post-doctoral fellowship of T.V.. We also thank the research group of Prof. Dr. Ludo Van Den Bosch and J.B. for their assistance on acquiring lipidomic data on our iPSC-SCP model.
In order to complete this thesis, help of following contributors has been essential. K.K. would like to thank the research group of E.W. of the Cardio & Organ Systems (COS) department at the Biomedical Research Institute (BIOMED, UHasselt) for their help during this project and their investment of time, effort and education. Mostly, K.K. would like to thank T.V. for the daily supervision, education on academic research, investment of time to provide highly relevant and insightful feedback, knowledge on research methods, trust and mentorship during this project. Additionally, K.K. is grateful for the opportunity to learn in the research group of I.L., and wants to thank him for his expert insights on the thesis topic. K.K. would also like to thank Jerome Hendriks for his advice during his senior internship. Moreover, K.K. would also especially like to thank H.J., Jolien Van Den Bosch and Lotte Alders for their help, guidance and support. Additionally, K.K. thanks E.W., J.B. and T.V. for the interesting discussions and debates on lipidomic research in CMT1A. Furthermore, K.K. is grateful for the contribution of S.H. and S.V. and L.M. towards data acquisition and experimental guidance during this study. K.K. would like to thank his fellow senior students Nathalie Dirckx, Sara Fieten and Aline Brillouet for their insights, support and daily deadline reminders during and after internship hours. Finally, K.K. specifically wants to thank his girlfriend and family for the continual support during his internship, but also throughout his bachelor degree, master degree, and the COVID-19 pandemic.

Author contributions – T.V., E.W. and I.L. conceived and designed the senior internship project and theoretical framework. T.V. supervised the study. K.K. and T.V. were involved in the daily planning of the project. K.K. and T.V. contributed to and carried out the research experiments with support from H.J., S.H., S.V. and K.L.. K.K. and T.V. performed the data analysis. T.V. provided reagents for the experiments. K.K. wrote the thesis and designed the figures, with support from T.V.. T.V. edited and reviewed the thesis. The authors affirm no competing interest.

REFERENCES

1. Kazamel M, Boes CJ. Charcot Marie Tooth disease (CMT): historical perspectives and evolution. J Neurol. 2015;262(4):801-5.
2. van Paassen BW, van der Kooi AJ, van Spaendonck-Zwarts KY, Verhamme C, Baas F, de Visser M. PMP22 related neuropathies: Charcot-Marie-Tooth disease type 1A and Hereditary Neuropathy with liability to Pressure Palsies. Orphanet J Rare Dis. 2014;9:38.
3. Vallat JM, Mathis S, Funalot B. The various Charcot-Marie-Tooth diseases. Curr Opin Neurol. 2013;26(5):473-80.
4. Pareyson D, Marchesi C. Diagnosis, natural history, and management of Charcot-Marie-Tooth disease. Lancet Neurol. 2009;8(7):654-67.
5. Boutary S, Echaniz-Laguna A, Adams D, Loisel-Duwattez J, Schumacher M, Massaad C, et al. Treating PMP22 gene duplication-related Charcot-Marie-Tooth disease: the past, the present and the future. Transl Res. 2021;227:100-11.
6. Pantera H, Shy ME, Svaren J. Regulating PMP22 expression as a dosage sensitive neuropathy gene. Brain Res. 2020;1726:146491.
7. Gautier B, Hajjar H, Soares S, Berthelot J, Deck M, Abbou S, et al. AAV2/9-mediated silencing of PMP22 prevents the development of pathological features in a rat model of Charcot-Marie-Tooth disease 1 A. Nat Commun. 2021;12(1):2356.
8. Hartmannsberger B, Doppler K, Stauber J, Schlotter-Weigel B, Young P, Sereda MW, et al. Intraepidermal nerve fibre density as biomarker in Charcot-Marie-Tooth disease type 1A. Brain Commun. 2020;2(1):fcaa012.
9. Berciano J, Gallardo E, Garcia A, Pelayo-Negro AL, Infante J, Combarros O. New insights into the pathophysiology of pes cavus in Charcot-Marie-Tooth disease type 1A duplication. J Neurol. 2011;258(9):1594-602.

10. Azevedo H, Pupe C, Pereira R, Nascimento OJM. Pain in Charcot-Marie-Tooth disease: an update. Arq Neuropsiquiatr. 2018;76(4):273-6.
11. Burns J, Ryan MM, Ouvrier RA. Quality of life in children with Charcot-Marie-Tooth disease. J Child Neurol. 2010;25(3):343-7.
12. Cordeiro JL, Marques W, Hallak JE, Osorio FL. Charcot-Marie-Tooth disease, psychiatric indicators and quality of life: a systematic review. ASN Neuro. 2014;6(3):185-92.
13. Taniguchi JB, Elui VM, Osorio FL, Hallak JE, Crippa JA, Machado-de-Sousa JP, et al. Quality of life in patients with Charcot-Marie-Tooth disease type 1A. Arq Neuropsiquiatr. 2013;71(6):392-6.
14. Amici SA, Dunn WA, Jr., Murphy AJ, Adams NC, Gale NW, Valenzuela DM, et al. Peripheral myelin protein 22 is in complex with alpha6beta4 integrin, and its absence alters the Schwann cell basal lamina. J Neurosci. 2006;26(4):1179-89.
15. Maier M, Berger P, Suter U. Understanding Schwann cell-neurone interactions: the key to Charcot-Marie-Tooth disease? J Anat. 2002;200(4):357-66.
16. Rosso G, Young P, Shahin V. Implications of Schwann Cells Biomechanics and Mechanosensitivity for Peripheral Nervous System Physiology and Pathophysiology. Front Mol Neurosci. 2017;10:345.
17. Taveggia C. Schwann cells-axon interaction in myelination. Curr Opin Neurobiol. 2016;39:24-9.
18. Mittendorf KF, Marinko JT, Hampton CM, Ke Z, Hadziselimovic A, Schlebach JP, et al. Peripheral myelin protein 22 alters membrane architecture. Sci Adv. 2017;3(7):e1700220.
19. Marinko JT, Kenworthy AK, Sanders CR. Peripheral myelin protein 22 preferentially partitions into ordered phase membrane domains. Proc Natl Acad Sci U S A. 2020;117(25):14168-77.
20. Lee S, Amici S, Tavori H, Zeng WM, Freeland S, Fazio S, et al. PMP22 is critical for actin-mediated cellular functions and for establishing lipid rafts. J Neurosci. 2014;34(48):16140-52.
21. Zhou Y, Miles JR, Tavori H, Lin M, Khoshbouei H, Borchelt DR, et al. PMP22 Regulates Cholesterol Trafficking and ABCA1-Mediated Cholesterol Efflux. J Neurosci. 2019;39(27):5404-18.
22. Di Tomaso MV, Vazquez Alberdi L, Olsson D, Cancela S, Fernandez A, Rosillo JC, et al. Colocalization Analysis of Peripheral Myelin Protein-22 and Lamin-B1 in the Schwann Cell Nuclei of Wt and TrJ Mice. Biomolecules. 2022;12(3).
23. Fortun J, Go JC, Li J, Amici SA, Dunn WA, Jr., Notterpek L. Alterations in degradative pathways and protein aggregation in a neuropathy model based on PMP22 overexpression. Neurobiol Dis. 2006;22(1):153-64.
24. Johnson JS, Roux KJ, Fletcher BS, Fortun J, Notterpek L. Molecular alterations resulting from frameshift mutations in peripheral myelin protein 22: implications for neuropathy severity. J Neurosci Res. 2005;82(6):743-52.
25. Tobler AR, Notterpek L, Naef R, Taylor V, Suter U, Shooter EM. Transport of Trembler-J mutant peripheral myelin protein 22 is blocked in the intermediate compartment and affects the transport of the wild-type protein by direct interaction. J Neurosci. 1999;19(6):2027-36.
26. Chernousov MA, Yu WM, Chen ZL, Carey DJ, Strickland S. Regulation of Schwann cell function by the extracellular matrix. Glia. 2008;56(14):1498-507.
27. Muppirala AN, Limbach LE, Bradford EF, Petersen SC. Schwann cell development: From neural crest to myelin sheath. Wiley Interdiscip Rev Dev Biol. 2021;10(5):e398.
28. Vega-Lopez GA, Cerrizuela S, Tribulo C, Aybar MJ. Neurocristopathies: New insights 150 years after the neural crest discovery. Dev Biol. 2018;444 Suppl 1:S110-S43.
29. Radomska KJ, Topilko P. Boundary cap cells in development and disease. Curr Opin Neurobiol. 2017;47:209-15.
30. Jessen KR, Mirsky R. Schwann Cell Precursors; Multipotent Glial Cells in Embryonic Nerves. Front Mol Neurosci. 2019;12:69.
31. Juliano RL, Haskill S. Signal transduction from the extracellular matrix. J Cell Biol. 1993;120(3):577-85.
32. Feltri ML, Scherer SS, Nemni R, Kamholz J, Vogelbacker H, Scott MO, et al. Beta 4 integrin expression in myelinating Schwann cells is polarized, developmentally regulated and axonally dependent. Development. 1994;120(5):1287-301.
33. Pellegatta M, De Arcangelis A, D'Urso A, Nodari A, Zambroni D, Ghidinelli M, et al. alpha6beta1 and alpha7beta1 integrins are required in Schwann cells to sort axons. J Neurosci. 2013;33(46):17995-8007.
34. Lefcort F, Venstrom K, McDonald JA, Reichardt LF. Regulation of expression of fibronectin and its receptor, alpha 5 beta 1, during development and regeneration of peripheral nerve. Development. 1992;116(3):767-82.
35. Pereira JA, Lebrun-Julien F, Suter U. Molecular mechanisms regulating myelination in the peripheral nervous system. Trends Neurosci. 2012;35(2):123-34.
36. Nodari A, Zambroni D, Quattrini A, Court FA, D'Urso A, Recchia A, et al. Beta1 integrin activates Rac1 in Schwann cells to generate radial lamellae during axonal sorting and myelination. J Cell Biol. 2007;177(6):1063-75.

37. Shen Y, Cheng Z, Chen S, Zhang Y, Chen Q, Yi S. Dysregulated miR-29a-3p/PMP22 Modulates Schwann Cell Proliferation and Migration During Peripheral Nerve Regeneration. Mol Neurobiol. 2022;59(2):1058-72.
38. Poitelon Y, Kopec AM, Belin S. Myelin Fat Facts: An Overview of Lipids and Fatty Acid Metabolism. Cells. 2020;9(4).
39. Fledrich R, Abdelaal T, Rasch L, Bansal V, Schutza V, Brugger B, et al. Targeting myelin lipid metabolism as a potential therapeutic strategy in a model of CMT1A neuropathy. Nat Commun. 2018;9(1):3025.
40. Visigalli D, Capodivento G, Basit A, Fernandez R, Hamid Z, Pencova B, et al. Exploiting Sphingo- and Glycerophospholipid Impairment to Select Effective Drugs and Biomarkers for CMT1A. Front Neurol. 2020;11:903.
41. Levental I, Levental KR, Heberle FA. Lipid Rafts: Controversies Resolved, Mysteries Remain. Trends Cell Biol. 2020;30(5):341-53.
42. Zhou Y, Borchelt D, Bauson JC, Fazio S, Miles JR, Tavori H, et al. Subcellular diversion of cholesterol by gain- and loss-of-function mutations in PMP22. Glia. 2020;68(11):2300-15.
43. Fledrich R, Stassart RM, Sereda MW. Murine therapeutic models for Charcot-Marie-Tooth (CMT) disease. Br Med Bull. 2012;102:89-113.
44. Juneja M, Burns J, Saporta MA, Timmerman V. Challenges in modelling the Charcot-Marie-Tooth neuropathies for therapy development. J Neurol Neurosurg Psychiatry. 2019;90(1):58-67.
45. Huang Z, Powell R, Phillips JB, Haastert-Talini K. Perspective on Schwann Cells Derived from Induced Pluripotent Stem Cells in Peripheral Nerve Tissue Engineering. Cells. 2020;9(11).
46. Martens W, Sanen K, Georgiou M, Struys T, Bronckaers A, Ameloot M, et al. Human dental pulp stem cells can differentiate into Schwann cells and promote and guide neurite outgrowth in an aligned tissue-engineered collagen construct in vitro. FASEB J. 2014;28(4):1634-43.
47. Sanen K, Paesen R, Luyck S, Phillips J, Lambrichts I, Martens W, et al. Label-free mapping of microstructural organisation in self-aligning cellular collagen hydrogels using image correlation spectroscopy. Acta Biomater. 2016;30:258-64.
48. Duval K, Grover H, Han LH, Mou Y, Pegoraro AF, Fredberg J, et al. Modeling Physiological Events in 2D vs. 3D Cell Culture. Physiology (Bethesda). 2017;32(4):266-77.
49. Lam D, Enright HA, Peters SKG, Moya ML, Soscia DA, Cadena J, et al. Optimizing cell encapsulation condition in ECM-Collagen I hydrogels to support 3D neuronal cultures. J Neurosci Methods. 2020;329:108460.
50. Sezgin E, Kaiser HJ, Baumgart T, Schwille P, Simons K, Levental I. Elucidating membrane structure and protein behavior using giant plasma membrane vesicles. Nat Protoc. 2012;7(6):1042-51.
51. Sezgin E, Waithe D, Bernardino de la Serna J, Eggeling C. Spectral imaging to measure heterogeneity in membrane lipid packing. Chemphyschem. 2015;16(7):1387-94.
52. Amici SA, Dunn WA, Jr., Notterpek L. Developmental abnormalities in the nerves of peripheral myelin protein 22-deficient mice. J Neurosci Res. 2007;85(2):238-49.
53. Poitelon Y, Matafora V, Silvestri N, Zambroni D, McGarry C, Serghany N, et al. A dual role for Integrin alpha6beta4 in modulating hereditary neuropathy with liability to pressure palsies. J Neurochem. 2018;145(3):245-57.
54. Previtali SC, Dina G, Nodari A, Fasolini M, Wrabetz L, Mayer U, et al. Schwann cells synthesize alpha7beta1 integrin which is dispensable for peripheral nerve development and myelination. Mol Cell Neurosci. 2003;23(2):210-8.
55. Heermann S, Schwab MH. Molecular control of Schwann cell migration along peripheral axons: keep moving! Cell Adh Migr. 2013;7(1):18-22.
56. Solovieva T, Bronner M. Reprint of: Schwann cell precursors: Where they come from and where they go. Cells Dev. 2021;168:203729.
57. Kaukua N, Shahidi MK, Konstantinidou C, Dyachuk V, Kaucka M, Furlan A, et al. Glial origin of mesenchymal stem cells in a tooth model system. Nature. 2014;513(7519):551-4.
58. Gaudreault M, Vigneault F, Gingras ME, Leclerc S, Carrier P, Germain L, et al. Transcriptional regulation of the human alpha6 integrin gene by the transcription factor NFI during corneal wound healing. Invest Ophthalmol Vis Sci. 2008;49(9):3758-67.
59. Linde A. The extracellular matrix of the dental pulp and dentin. J Dent Res. 1985;64 Spec No:523-9.
60. Furlan A, Adameyko I. Schwann cell precursor: a neural crest cell in disguise? Dev Biol. 2018;444 Suppl 1:S25-S35.
61. Hagedorn L, Suter U, Sommer L. P0 and PMP22 mark a multipotent neural crest-derived cell type that displays community effects in response to TGF-beta family factors. Development. 1999;126(17):3781-94.
62. Wulf P, Bernhardt RR, Suter U. Characterization of peripheral myelin protein 22 in zebrafish (zPMP22) suggests an early role in the development of the peripheral nervous system. J Neurosci Res. 1999;57(4):467-78.

63. Amaro M, Reina F, Hof M, Eggeling C, Sezgin E. Laurdan and Di-4-ANEPPDHQ probe different properties of the membrane. J Phys D Appl Phys. 2017;50(13):134004.
64. Yu W, So PT, French T, Gratton E. Fluorescence generalized polarization of cell membranes: a two-photon scanning microscopy approach. Biophys J. 1996;70(2):626-36.
65. Bogie JFJ, Grajchen E, Wouters E, Corrales AG, Dierckx T, Vanherle S, et al. Stearoyl-CoA desaturase-1 impairs the reparative properties of macrophages and microglia in the brain. J Exp Med. 2020;217(5).
66. Fagone P, Jackowski S. Phosphatidylcholine and the CDP-choline cycle. Biochim Biophys Acta. 2013;1831(3):523-32.
67. Levental I, Veatch S. The Continuing Mystery of Lipid Rafts. J Mol Biol. 2016;428(24 Pt A):4749-64.
68. Santos G, Diaz M, Torres NV. Lipid Raft Size and Lipid Mobility in Non-raft Domains Increase during Aging and Are Exacerbated in APP/PS1 Mice Model of Alzheimer's Disease. Predictions from an Agent-Based Mathematical Model. Front Physiol. 2016;7:90.
69. Wang N, Westerterp M. ABC Transporters, Cholesterol Efflux, and Implications for Cardiovascular Diseases. Adv Exp Med Biol. 2020;1276:67-83.
70. Dawaliby R, Trubbia C, Delporte C, Noyon C, Ruysschaert JM, Van Antwerpen P, et al. Phosphatidylethanolamine Is a Key Regulator of Membrane Fluidity in Eukaryotic Cells. J Biol Chem. 2016;291(7):3658-67.
71. Olzmann JA, Carvalho P. Dynamics and functions of lipid droplets. Nat Rev Mol Cell Biol. 2019;20(3):137-55.
72. Penno A, Hackenbroich G, Thiele C. Phospholipids and lipid droplets. Biochim Biophys Acta. 2013;1831(3):589-94.
73. Smolic T, Zorec R, Vardjan N. Pathophysiology of Lipid Droplets in Neuroglia. Antioxidants (Basel). 2021;11(1).
74. de Macedo CS, Lara FA, Pinheiro RO, Schmitz V, de Berredo-Pinho M, Pereira GM, et al. New insights into the pathogenesis of leprosy: contribution of subversion of host cell metabolism to bacterial persistence, disease progression, and transmission. F1000Res. 2020;9.
75. Lewandowski CT, Laham MS, Thatcher GRJ. Remembering your A, B, C's: Alzheimer's disease and ABCA1. Acta Pharm Sin B. 2022;12(3):995-1018.
76. Maqdasy S, Trousson A, Tauveron I, Volle DH, Baron S, Lobaccaro JM. Once and for all, LXRalpha and LXRbeta are gatekeepers of the endocrine system. Mol Aspects Med. 2016;49:31-46.
77. Janani C, Ranjitha Kumari BD. PPAR gamma gene--a review. Diabetes Metab Syndr. 2015;9(1):46-50.
78. Kidani Y, Bensinger SJ. Liver X receptor and peroxisome proliferator-activated receptor as integrators of lipid homeostasis and immunity. Immunol Rev. 2012;249(1):72-83.
79. Rao MJ, Goodman JM. Seipin: harvesting fat and keeping adipocytes healthy. Trends Cell Biol. 2021;31(11):912-23.
80. Ito D, Suzuki N. Seipinopathy: a novel endoplasmic reticulum stress-associated disease. Brain. 2009;132(Pt 1):8-15.
81. Castelnovo LF, Bonalume V, Melfi S, Ballabio M, Colleoni D, Magnaghi V. Schwann cell development, maturation and regeneration: a focus on classic and emerging intracellular signaling pathways. Neural Regen Res. 2017;12(7):1013-23.
82. Hilkens P, Gervois P, Fanton Y, Vanormelingen J, Martens W, Struys T, et al. Effect of isolation methodology on stem cell properties and multilineage differentiation potential of human dental pulp stem cells. Cell Tissue Res. 2013;353(1):65-78.
83. Burg T, Rossaert E, Moisse M, Van Damme P, Van Den Bosch L. Histone Deacetylase Inhibition Regulates Lipid Homeostasis in a Mouse Model of Amyotrophic Lateral Sclerosis. Int J Mol Sci. 2021;22(20).
84. Baron DM, Fenton AR, Saez-Atienzar S, Giampetruzzi A, Sreeram A, Shankaracharya, et al. ALS-associated KIF5A mutations abolish autoinhibition resulting in a toxic gain of function. Cell Rep. 2022;39(1):110598.

SUPPLEMENTARY MATERIALS AND METHODS

DPSC isolation and DPSC(-PMP22) cell culture – DPSCs were obtained from a patient (n=1) undergoing a tooth extraction procedure for orthodontic reasons at Ziekenhuis Oost-Limburg (ZOL, Genk, Belgium). Written informed consent was obtained prior to the procedure. The dental pulp was obtained by mechanical fracturing, and subsequent gentle isolation with forceps to maintain cell viability. The dental pulp was rinsed in standard DPSC medium (α-MEM with 2mM L-glutamine, 100 U/ml penicillin & streptomycin and 10% FBS) and minced into 1-2 mm^3 sized fragments. DPSCs were then isolated through the explant method (82). In brief, dental pulp tissue fragments were placed in 6-well plates in DPSC medium for 48-72h, after which the DPSCs were able to grow out of the dental pulp tissue. At 70-80% confluence, DPSCs were harvested with 0.05% trypsin/EDTA (Sigma) and seeded for further use.

PMP22 transduction into DPSCs – DPSCs were seeded in a 24-well plate (5000 cells/well) in minimal DPSC medium (α-MEM with 5% FBS). DPSC medium was changed for transduction medium (α-MEM with 5% FBS and 8 µg/ml polybrene) and lentiviral particles (containing the *PMP22*-plasmid construct; 8-10 µl/well) were added to the medium for 7 hours. Medium was subsequently changed to minimal DPSC medium and when confluent, puromycin (2 µg/ml) was added to the cells. After cell death of the negative controls, medium was changed to α-MEM with 10% FCS. After 48-72 hours, cells were pooled to T25 culture flasks for further use in standard DPSC medium.

RNA isolation and cDNA synthesis – cells were cultured at a density of 30 000 cells in 24 well plates. After 3-4 days when confluence is reached, cell lysates are collected in Qiazol (QIAGEN) and stored at -80°C until further usage. Cells were then kept on ice in glycogen. Next, 100 µl chloroform was added and the samples were centrifugated at room temperature for 5 min at 200 rpm. The aqueous phase top layer of fluid, containing mRNA, was brought over in new glycogen and a sufficient amount of 2-isopropanol was added to double the volume. Subsequently, the samples were incubated for 30 min at room temperature, followed by centrifugation at 4°C for 10 min at 14000 rpm. After removing the supernatant, the RNA pellet was washed twice in 800 µl ethanol, vortexed and centrifuged at 4°C for 10 min at 14000 rpm. This was followed by full removal of the supernatant. The remaining pellet was dried for 20 min in a Thermoblock heater, followed by suspension in sterile MilliQ. After vortexing and incubation for 10 min, twice, RNA concentration was measure using the NanoDrop® ND-1000 spectrophotometer. Finally, DNA-free water and Qscript cDNA supermix (Quanta Biosciences) was added to the samples and PCR was performed to form the cDNA. DNA-free water was added to reach equal concentrations in every sample.

Lipid extraction and mass spectrometry data acquisition - Lipid extraction and mass spectrometry thereof was performed by the group of prof. dr. Ludo Van Den Bosch, similar to the method described in Burg et al (83). In brief, lipid extraction was performed via a two-step chloroform/methanol procedure. Samples were then spiked with a lipid standard mixture containing lipid species shown in figure 6a. After lipid extraction, the organic phase was brought onto an infusion plate and dried, using a speed vacuum concentrator. The dry lipid extract was resuspended 1) in 7.5 mM ammonium actetate in a 1:2:4 mixture of chloroform, methanol and propanol, respectively and 2) in 33% ethanol solution of a 0.003:5:1 mixture of methylamine, chloroform and methanol, respectively. Samples were directly infused on a QExactive mass spectrometer (Thermo Scientific, Waltham, MA, USA) with a TriVersa NanoMate ion source (Advion Biosciences, Ithaca, NY, USA). Both in positive and negative ion modes samples were analyzed with a resolution of Rm/z = 200 = 280 000 for MS and Rm/z = 200 = 17 500 for MSMS experiments in a single acquisition. Data analysis was done with LipidXplorer, further optimized in-house by the research group of Prof. dr. Ludo Van Den Bosch. nmoles of lipids in a lipid class were normalized to the sample DNA (mg).

RNA sequencing analysis – RNA sequencing data was kindly provided by the group of prof. dr. Ludo van den Bosch and performed similar to the methodology used in Baron et al (84). After RNA isolation, samples were sent to the Nucleomics Core (VIB, Leuven, Belgium) for analysis of the sample RNA integrity (≥ 8) using a Bioanalyzer (Agilent). Next, Trueseq total stranded RNA libraries were prepared and sequenced using a Illumina NextSeq 500 system (Illumina, San Diego, USA). Libraries were sequenced with a high output paired end with 75 bp reads (approximately 50 million reads per sample). Mapping of the reads was done with STAR aligner on the latest human genome build. Salmon was used for the count

of the reads in order to estimate transcript and gene expression. Differential expression of coding genes and transcripts was performed with edgeR. Transcripts with an FDR-adjusted P-value <0.05 (FDR Benjamini-Hochberg correction) and altered expression of 30% were considered significantly differentially expressed.

Cholesterol and DiI myelin uptake assays - For efflux measurement, iPSC-SCPs were exposed to apoA-I (50µg/ml) in serum- and phenol-free medium for 4 hours total. Medium supernatant was isolated (extracellular cholesterol) and diluted in reaction buffer (1:1) and cells were scraped in Amplex reaction buffer (intracellular cholesterol). For cellular cholesterol content, cells were supplemented with reaction buffer and subsequently scraped from the bottom. Both efflux and cellular cholesterol levels were determined with the Amplex™ Red Cholesterol Assay Kit, performed according to the manufacturers' protocol. Fluorescence levels were measured using a FLUOstar OPTIMA microplate reader. Cholesterol efflux was subsequently determined by dividing supernatant fluorescence by the total fluorescence in the cells and supernatant. For myelin uptake analysis, human CNS Myelin (100 µg/ml) was labelled with 1,1"-diotadecyl-3,3,3',3',-tetramethylindocarbocyanide perchlorate (DiI; Sigma-Aldrich). iPSC-SCPs were stimulated with DiI-myelin for 30 min. Flow cytometry was used to assess overall cellular DiI uptake.

Supplementary Table 1 – Primary and secondary antibodies used for immunocytochemistry.

Primary antibodies

Target	Species	Ref. No.	Dilution	Isotype	Manufacturer
Integrin alpha 6	ab20142	mouse	1/250	IgG2b	Abcam, Cambridge, UK
Integrin beta 1	ab179471	rabbit	1/250	IgG	Abcam, Cambridge, UK
Integrin beta 4	ab29042	mouse	1/250	IgG1	Abcam, Cambridge, UK
PMP22	bs-03235r-TR	rabbit	1/250	IgG	Bioss, Boston, USA
Integrin beta 1	34971S	rabbit	1/300	IgG	Cell Signaling Technology, Massachusetts
PMP22	ab15506	Rabbit	1/300	IgG	Abcam, Cambridge, UK
MPZ	ab183868	rabbit	1/200	IgG	Abcam, Cambridge, UK
Oct-6	ab221964	rabbit	1/200	IgG	Abcam, Cambridge, UK
S100	ab14849	mouse	1/200	IgG	Abcam, Cambridge, UK
Sox10	ab180862	rabbit	1/200	IgG	Abcam, Cambridge, UK

Secondary antibodies

Target	Species	Ref. No.	Dilution	Isotype	Manufacturer
Alexa 488	A21206	Donkey anti-mouse	1/300	IgG	Invitrogen by Thermo Fisher Scientific, Life Technologies Corporation, Oregon, Eugene, USA
Alexa 555	A21425	Goat anti-mouse	1/300	F(ab')2	
Alexa 555	A31572	Donkey anti-rabbit	1/300	IgG	
Alexa 488	A21202	Donkey anti-mouse	1/300	IgG	

PMP22: Peripheral Myelin Protein 22; MPZ: Myelin Protein Zero; Oct-6: Octamer transcription factor 6; S100: Calcium-binding protein B; Sox10: SRY-Box Transcription Factor 10

Supplementary Table 2 – List of primers used for qPCR.

Gene transcript target	Full name	Primer sequences
PMP22	Peripheral Myelin Protein 22	F: TTTGGCCGGGCAGAAAC R: GAGACGAACAGCAGCACCA
ITGA5	Integrin alpha 5	F: GCCTGTGGAGTACAAGTCCTT R: AATTCGGGTGAAGTTATCTGTGG
ITGA6	Integrin alpha 6	F: ATGCACGCGGATCGAGTTT R: TTCCTGCTTCGTATTAACATGCT
ITGA7	Integrin alpha 7	F: CAGCGAGTGGACCAGATCC R: CCAAAGAGGAGGTAGTGGCTATC
ITGB1	Integrin beta 1	F: CCTACTTCTGCACGATGTGATG R: CCTTTGCTACGGTTGGTTACATT
TAZ (WWTR1)	WW domain-containing Transcription Regulator protein 1	F: TCCCAGCCAAATCTCGTGATG R: AGCGCATTGGGCATACTCAT
YAP1	Yes-associated Protein 1	F: TAGCCCTGCGTAGCCAGTTA R: TCATGCTTAGTCCACTGTCTGT
FAK (PTK2)	Focal Adhesion Kinase (Protein Tyrosine Kinase 2)	F: GCTTACCTTGACCCCAACTTG R: ACGTTCCATACCAGTACCCAG
PXN	Paxillin	F: CTGCTGGAACTGAACGCTGTA R: GGGGCTGTTAGTCTCTGGGA
SLC44A1 (CTL1)	Solute Carrier Family 44 Member 1 (Choline transporter-like protein 1)	F: GGACCGTAGCTGCACAGAC R: GCCACAAATAAATCCCATCCCA
GLB1	Galactosidase beta 1	F: TATACTGGCTGGCTAGATCACTG R: GGCAAAATTGGTCCCACCTATAA
BSCL2	Berardinelli-Seip congenital lipodystrophy 2 (seipin)	F: ATGGTCAACGACCCTCCAGTA R: GCTGACTGTCGGCATATAGGAA
CADM4 (NECL4)	Cell Adhesion Molecule 4 (Nectin-Like 4)	F: GCCGTCTGCACCAGTATGAT R: CTGGAAACGCTCATCCTTCAA

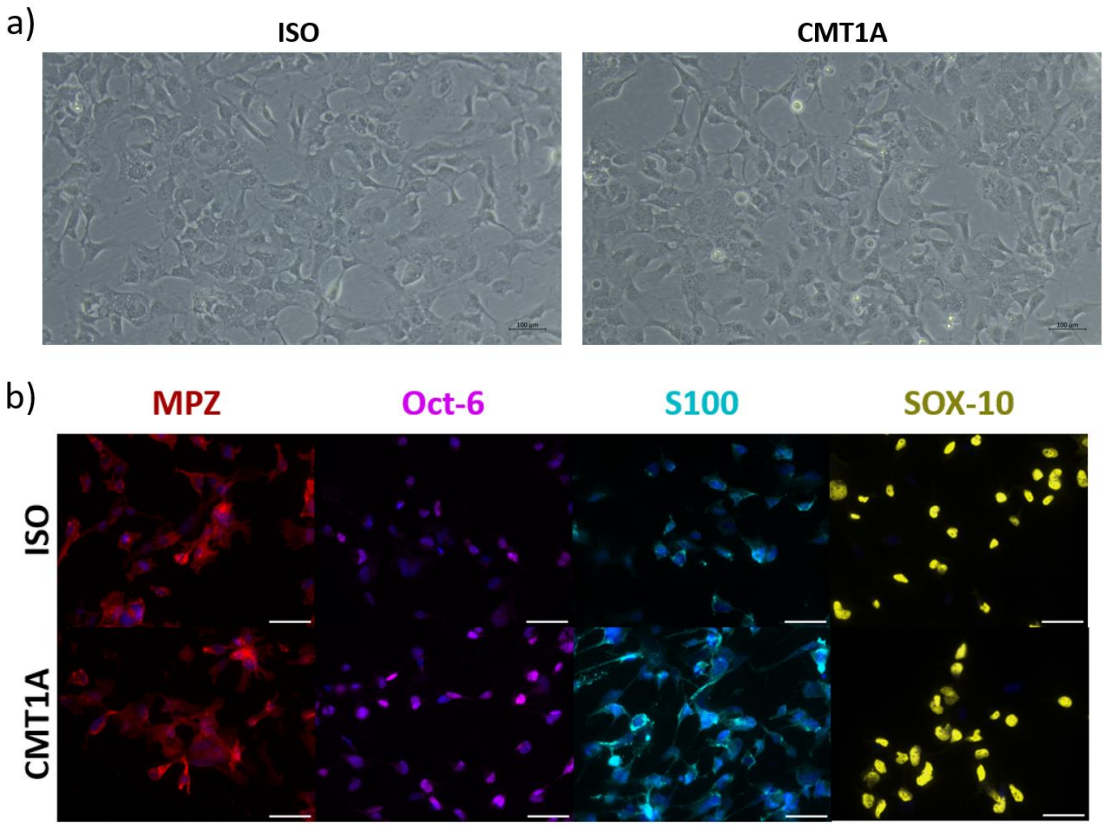

Supplementary Figure 1 – a) Representative image of a isogenic and CMT1A Schwann cell precursor-like induced pluripotent stem cell (iPSC-SCP). iPSC-SCPs usually have a multipolar, extended cellular morphology and form distinct groups in culture. Scale bar = 100 µm. b) Representative images of Schwann cell precursor/Schwann cell lineage marker expression. MPZ = red; Oct-6 = purple; S100 = cyan; SOX-10 = yellow; DAPI counterstain = dark blue. scale bar = 50 µm.

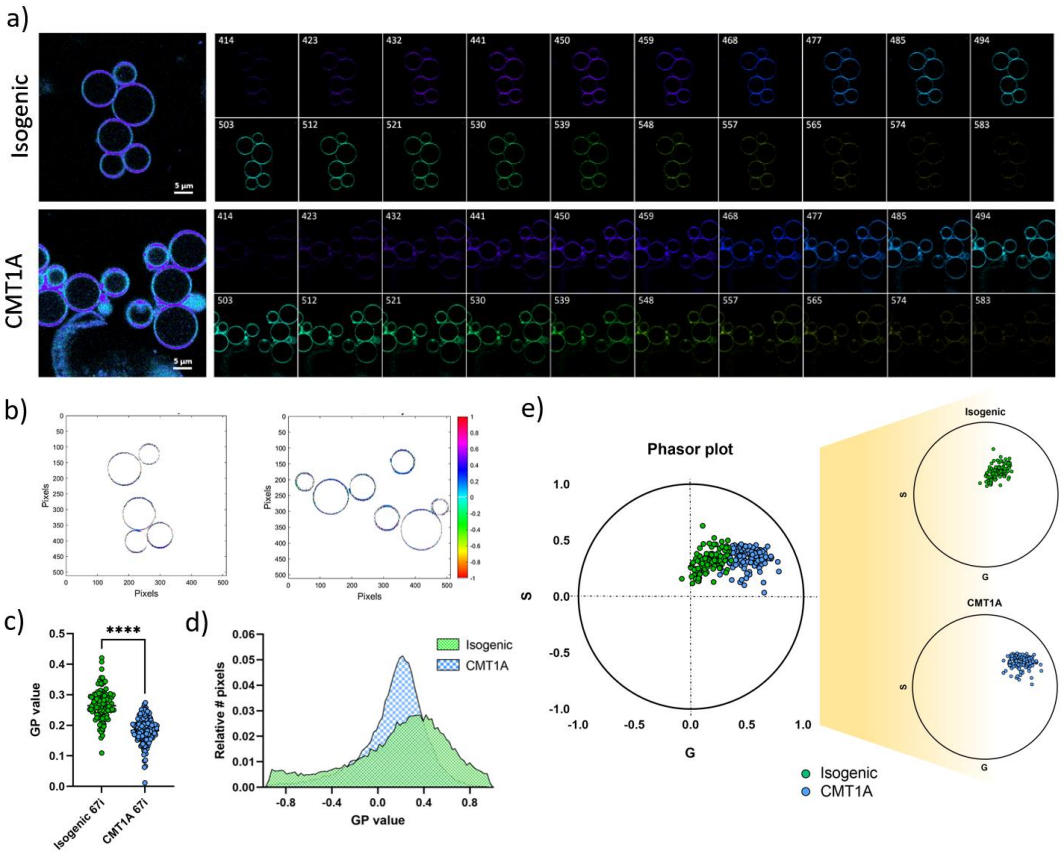

Supplementary Figure 2 –Laurdan labelled GPMVs from CMT1A iPSC-SCPs reveal a decreased membrane lipid generalized polarization. a) Representative images of the Laurdan-labelled ISO and CMT1A SCP GPMVs spectral profile (414-583nm; 9nm interval). b) GP value per pixel in ISO and CMT1A iPSC-SCP GPMVs. c) Quantitative Laurdan GP value comparison of isogenic and CMT1A SCPs. Mann-Whitney U test; P-value: ****<0.0001. d) Laurdan GP value distribution of isogenic and CMT1A SCPs. e) Phasor plot distribution of isogenic and CMT1A iPSC-SCP GPMV Laurdan emission spectra. MANOVA-analysis reveals a very large effect of ISO/CMT categorization on the phasor plot data distribution (p-value < 0.0001; Partial Eta Squared = 0.73).

Supplementary Table 3 – List of abbreviations used.

Abbreviation	Explanation
CMT	Charcot-Marie-Tooth disease
HMSN	Hereditary motor and sensory neuropathy
PNS	Peripheral nervous system
PMP22	Peripheral myelin protein 22
TrJ	Trembler-J mouse model
C22	C22-mouse model
ECM	Extracellular matrix
NCC	Neural crest cells
CNS	Central nervous system
SCP	Schwann cell precursor
iSC	Immature Schwann cell
Pro-SC	Pro-myelinating Schwann cell
DRG	Dorsal root ganglia
Rac1	Ras-related C3 botulinum toxin substrate 1
F-actin	Filamentous actin
GLB1	Galactosidase 1
ABCA1	ATP-binding cassette transporter A1
ApoE	Apolipoprotein E
iPSC	Induced pluripotent stem cell
DPSC	Human dental pulp stem cell
DPSC-SC	Dental pulp stem cell-Schwann cells
iPSC-SCP (SCP)	Induced pluripotent stem cell-Schwann cell precursor
DPSC-PMP22	PMP22-overexpressing DPSCs
HNPP	Hereditary neuropathy with liability to pressure palsies
GPMV	Giant plasma membrane vesicle
PC	Phosphatidylcholine
PE	Phosphatidylethanolamine
PS	phosphatidylserine
LXR	Liver X receptor
PCTP	Phosphatidylcholine transfer protein
ORP5	Oxysterol-binding protein-related protein 5
ORP8	Oxysterol-binding protein-related protein 8
PPARg	Peroxisome proliferator-activated receptor gamma
Eth	Ethanolamine
Cho	Choline
ETNK	Ethanolamine kinase
CHK	Choline kinase
P-Eth	Phosphoethanolamine
P-Cho	Phosphocholine
ECT	CTP-phosphoethanolamine cytidylyltransferase
CCT	CTP:phosphocholine cytidylyltransferase
CDP-Eth	CDP-ethanolamine
CDP-Cho	CDP-choline
CEPT	Choline/ethanolaminephosphotransferase
CPT	Choline phosphotransferase
PSS1	Phosphatidylserine synthase 1
PSS2	Phosphatidylserine synthase 2
AP	Action potential
ISO	Isogenic

TIRF	Total internal reflection fluorescence
HEPES	N-(2-Hydroxyethyl)piperazine-N'-(2-ethanesulfonic acid)
DTT	Dithiothreitol
GP	Generalized polarization
MEM	Minimal essential medium
TPE	Two-photon excitation
SHG	Second harmonic generation
GAPDH	Glyceraldehyde 3-phosphate dehydrogenase
RPL13A	60S ribosomal protein L13a
YWHAZ	14-3-3 protein zeta/delta
CYCA	Cyclophilin A
ddPCR	Digital PCR
YAP-1	Yes-associated protein 1
TAZ	transcriptional coactivator with PDZ-binding motif (*WWTR1*-gene)
FAK	Focal adhesion kinase
PXN	Paxillin
CTL1	Solute Carrier Family 44 Member 1
CADM4	Cell Adhesion Molecule 4
ApoA-I	Apolipoprotein AI
DiI	1,1"-diotadecyl-3,3,3',3',-tetramethylindocarbocyanide perchlorate
MBCD	Methyl-β-cyclodextrine
BSCL2	Berardinelli-Seip congenital lipodystrophy 2 (Seipin)